Article:
Esmaili, H, Kowsari, E, Sarabadani Tafreshi, S et al. (3 more authors) (2022) TiO2 nanoarrays modification by a novel Cobalt-heteroatom doped graphene complex for photoelectrochemical water splitting: An experimental and theoretical study. Journal of Molecular Liquids, 356. 118960. ISSN 0167-7322

https://doi.org/10.1016/j.molliq.2022.118960

TiO_2 nanoarrays modification by a novel Cobalt-heteroatom doped graphene complex for photoelectrochemical water splitting: an experimental and theoretical study

Hamed Esmaili[a], Elaheh Kowsari[a*], Saeedeh Sarabadani Tafreshi[a], Seeram Ramakrishna[b], Nora H. de leeuw[c,d] and Majid Abdous[a]

[a] *Amirkabir university of technology, Department of chemistry, Tehran, Iran*

[b] *Center for nanofibers& nanotechnology, Department of Mechanical Engineering, National University of Singapore, Singapore 117576*

[c] *School of Chemistry, Cardiff University, Main Building, Park Place, Cardiff CF10 3AT, United Kingdom*

[d] *School of Chemistry, University of Leeds, Leeds LS2 9JT, United Kingdom*

[*] Corresponding author's email: e_kowsari@yahoo.com (E.Kowsari) and seeram@nus.edu.sg (S.Ramakrishna)

Abstract

Different graphene structures have received much attention due to their unique chemical and electron properties. In this report, we use heteroatom-doped graphene to coordinate Co^{2+} for use in photoelectrochemical cells. Flower-like TiO_2 photoelectrode morphology was used as a semiconductor. Its surface was covalently modified with Co^{2+} coordinated nitrogen and sulfur-doped graphene quantum dot (S, N-GQD). S, N-GQD was used to improve visible light absorption and electron transport properties. Also, cobalt ions were coordinated with pyridinic nitrogen in the GQD structure and, like the cobalt-bipyridine complexes, acted as a catalyst for the water oxidation reaction. The modified photoelectrode significantly improved cell performance and resulted in a photocurrent density of 1.141 mA/cm^2. To study the electronic structure of the compounds in more detail, we also used density functional theory (DFT) calculations. The obtained results confirmed the effective interactions of cobalt and S, N-GQD, and showed the energy levels and band gaps in agreement with the experimental results. This study led to the presentation

of a new and robust strategy to improve the optical and catalytic performance of TiO_2 nanoarrays in photoelectrochemical cells.

Keywords: Photoelectrochemical water splitting, S, N-doped graphene quantum dots, TiO_2 nanorod arrays

1. Introduction

The production of green, low-cost, storable, and renewable chemical fuels is a significant challenge for scientists and researchers[1,2]. The ideal way to generate energy is to use low-cost energy sources and more available raw materials. Nature tells us that the best source is solar energy, and the most readily available raw material is water. Therefore, recently, solar water splitting has attracted researchers' attention Due to creating a bridge between electrochemical and photocatalytic processes[3–6]. Using photoelectrochemical (PEC) cells is one of the best ways to use sunlight to drive the water-splitting reaction. This process has faced various challenges since its introduction, but researchers always have good prospects for it in the future[7–11]. The mechanism of action is based on advancing oxidation and reduction reactions through electrons and holes created by photons received on the surface of the semiconductor. Although this technique has proposed a new path for hydrogen production, it suffers from significant shortcomings such as low efficiency and expensive materials for use in photoelectrodes. Various metal oxides and nitrides such as α-Fe_2O_3, GaN, and WO_3 are used as photoanodes in these cells[12–16]. TiO_2 is a unique material among these semiconductors because of its outstanding features, such as low price, high chemical stability, availability, and non-toxicity and for these reasons, it has often been considered by researchers for use as the solar hydrogen production[17–26]. Of course, the toxicity of TiO_2 also depends on its size and structure. However, this semiconductor's vast energy bandgap and fast charge carrier recombination have

challenged its use in the visible area[27,28]. Hence, various methods have been proposed to overcome these limitations, which utilize dyes[29–32], co-catalysts[33], morphology modification[34], and doping[35] as part of these efforts. Using 1-D single-crystal TiO_2, such as nanorods, has received much attention due to its easy synthesis, uniformity, high electron transfer rate, scalability, and reduced charge recombination[36–38]. Liu et al.[39] directly synthesized single-phase TiO_2 nanorods on the FTO conductive substrate in a strongly acidic environment by hydrothermal method. It is easy to obtain an optimal length of nanorods with the best current efficiency[38]. In addition to nanorods, various other morphologies such as nanotubes and urchin-like were synthesized for TiO_2. Morphologies that, in addition to providing better pathways for electron transport, can better absorb light due to increased light inner reflection.

Numerous materials have been used as sensitizers for TiO_2. From ruthenium complexes to natural dyes, all have come with the help of TiO_2 to overcome the defect of visible light absorption of this semiconductor. However, high prices and low efficiency are among the disadvantages of various sensitizers. For example, Park et al. Used gold nanoparticles to improve visible light absorption and photoelectrochemical activity of TiO_2[40], or Swierk et al. Used ruthenium complex as a sensitizer for TiO_2 semiconductors[41]. Since gold and ruthenium are both expensive elements, the need to use metal free, inexpensive, and available sensitizers instead of these compounds has always been considered by researchers. Using quantum dots and TiO_2 to overcome low visible light absorption was one of the most practical ideas to increase cell efficiency. Graphene quantum dots (GQDs), like graphene oxides, is one of the most important materials for use in photovoltaic cells due to their optical and electrical properties[42–48] as well as their functionalization[49–58]. The GQDs have advantages such as outstanding light absorption in the visible region, non-toxicity, inexpensiveness, easy synthesis, and good electron transport capability. Furthermore, adding other elements into these compounds' structures as dopants has improved its photocatalytic properties[59]. However, the graphene quantum dots' high solubility in water has limited their use in photoelectrochemical cells to conduct water-splitting reactions.

In addition to light-absorbing materials, using an oxygen evolution reaction (OER) catalyst also significantly affects PEC performance [60–63]. Among the appropriate catalysts for this reaction, such as IrO_2 and FeOOH, cobalt compounds and, in particular, cobalt complexes have been widely used[64,65]. Ruthenium and iridium-based catalysts, in addition to their high cost, have complex structures that pose challenges in their application in all fields. Duan et al., For example, have proposed a molecular water oxidation catalyst based on the ruthenium complex[66], which, in addition to excellent performance, faces challenges such as high cost and complexity of structure and synthesis. Swierk et al. Also used iridium oxide as a catalyst for water oxidation[41]. This combination, despite its good performance, is still a component of high-priced compounds. Cobalt-containing compounds as inexpensive materials, such as cobalt phosphide and cobalt sulfide, have a very positive effect on electron transport from the electrode-electrolyte interface and often accelerate the oxidation process of water by creating appropriate interfaces. Some of these compounds are inexpensive and efficiently synthesized[67–70]. Of course, there still seems to be a great deal to study.

This study reports a new strategy for functionalizing TiO_2 nanoarrays surface with Co^{2+} by coordination with S, N-codoped graphene quantum dot. The application of this complex improved both the semiconductor optical and catalytic properties. On the one hand, the addition of sulfur and nitrogen to the quantum dot structure improved the visible light absorption of the system. On the other hand, the cobalt-pyridine structure of Quantum Dot accelerates the oxidation reaction of water through the formation of the cobalt (IV) intermediate. To prevent S, N-GQD, and cobalt ions from dissolution in the aqueous electrolyte, the nanoarrays surface was modified with the aminosilane compound. Then, Coordinated Cobalt with S, N-GQD was bonded to the nanoarrays modified surface using dicyclohexylcarbodiimide (DCC) and dimethylamino pyridine (DMAP). This system exhibited significant PEC water splitting performance improvement by photocurrent density of 1.141 mA/cm^2 at 1.23 V vs. RHE. Furthermore, the covalently modified photoanode showed a very stable current density compared to a non-covalent modified

electrode. In addition to structural analyzes density functional theory calculations were performed to investigate the interaction of cobalt ions with quantum dot graphene. HOMO and LUMO levels of the compounds used in this study were accurately calculated and compared with the values obtained from experimental analyzes.

2. Experimental

2.1 Materials and methods

Citric acid (CA), thiourea, urea, Cobalt chloride Hexahydrate($CoCl_2.6H_2O$), Hydrochloric acid (HCl 37%), Ethanol, Acetic Acid (HOAc), N, N-Dimethylformamide (DMF 99%) was purchased from Merck, and titanium(IV) isopropoxide (TTIP), (3-aminopropyl)trimethoxysilane (APTMS), dicyclohexylcarbodiimide (DCC) and dimethylamino pyridine (DMAP) purchased from Sigma-Aldrich company. All of the reagents were used without further purification.

The TiO_2 nanoarrays (TNR) were grown by hydrothermal method from a mixed acid media[48]. In a typical process, the mixture of 8 ml of HOAc, 8 ml of deionized water, 4 ml of HCl 37%, and 0.8 ml of TTIP was stirred into a container. The mixture was then stirred for a few minutes until completely homogenized and poured into a 100 ml Teflon-lined stainless steel autoclave. Then, a 2×1 cm^2 piece of FTO substrate, prepared by ultrasonication in a mixture of water/detergent and ethanol, was put into the reactor. The reaction was conducted at 180 °C for 4 hours. After hydrothermal synthesis, the autoclave was cooled to room temperature slowly, and the FTO glass substrate was washed with double distilled water and annealed at 450 °C for 30 minutes.

To amine functionalization of TiO_2 (NH_2-TiO_2) surface, 100 µL of APTMS was added to the mixture of 10 ml of EtOH and 50 µL of deionized water and stirred for 10 min. Then the FTO-coated TiO_2 nanoarrays were placing in the solution, and stirring stopped. The reaction mixture was heated at 65 °C for 30 minutes. The FTO was removed from the mixture and, after washing with EtOH, dried at ambient temperature for three hours.

The hydrothermal method was used for graphene quantum dot synthesis[71]. Typically, In a 100 ml Teflon-lined stainless steel autoclave, 25 ml of deionized water, 1.05 g of CA, and 1.15 g of thiourea were poured and stirred until complete dissolution. After sealing the autoclave, the synthesis was performed for 6 hours at 180 °C. After cooling to room temperature, ethanol was added to the reaction product. Then, by centrifugation at 8000 rpm for 15 minutes, the product was separated from the excess impurities and dried at 100 °C for five hours. Finally, 1.37 g of dry product was obtained, which shows a 63% efficiency for synthesis. In addition to S, N-GQD, N-Doped graphene quantum dot (N-GQD) was synthesized using citric acid and urea instead of thiourea in the same way and the same amounts for all materials to be used as a comparison in the analyzes. 1.46 grams of N-GQD was obtained from the product, which shows a 67% efficiency for the reaction. Finally, for modification of TNR surface with Co-S,N-GQD (TNR-Co-S,N-GQD), 0.2 g S, N-GQD (for TNR-Co-S,N-GQD$_{0.2}$), and 25 mg $CoCl_2.6H_2O$ were added to 10 ml of EtOH and stirred for 1 hour. In another container, 20 mg DCC, 20 mg DMAP, and 10 ml of DMF were mixed for 30 minutes. Then the functionalized FTO was put in the mixture, and stirring was stopped. The first mixture was poured slowly in the second and heated at 40 °C for 5 hours. After that, the FTO was removed, rinsed with EtOH, and dried at 100 °C for 4 hours. In order to investigate of the GQD quantitative effect on the overall efficiency of the cell, two other electrodes with 0.1 g (TNR-Co-S,N-GQD$_{0.1}$) and 0.4g (TNR-Co-S,N-GQD$_{0.4}$) of S,N-GQD were made.

All the synthesis steps and surface modification of the photoelectrode are shown in scheme 1.

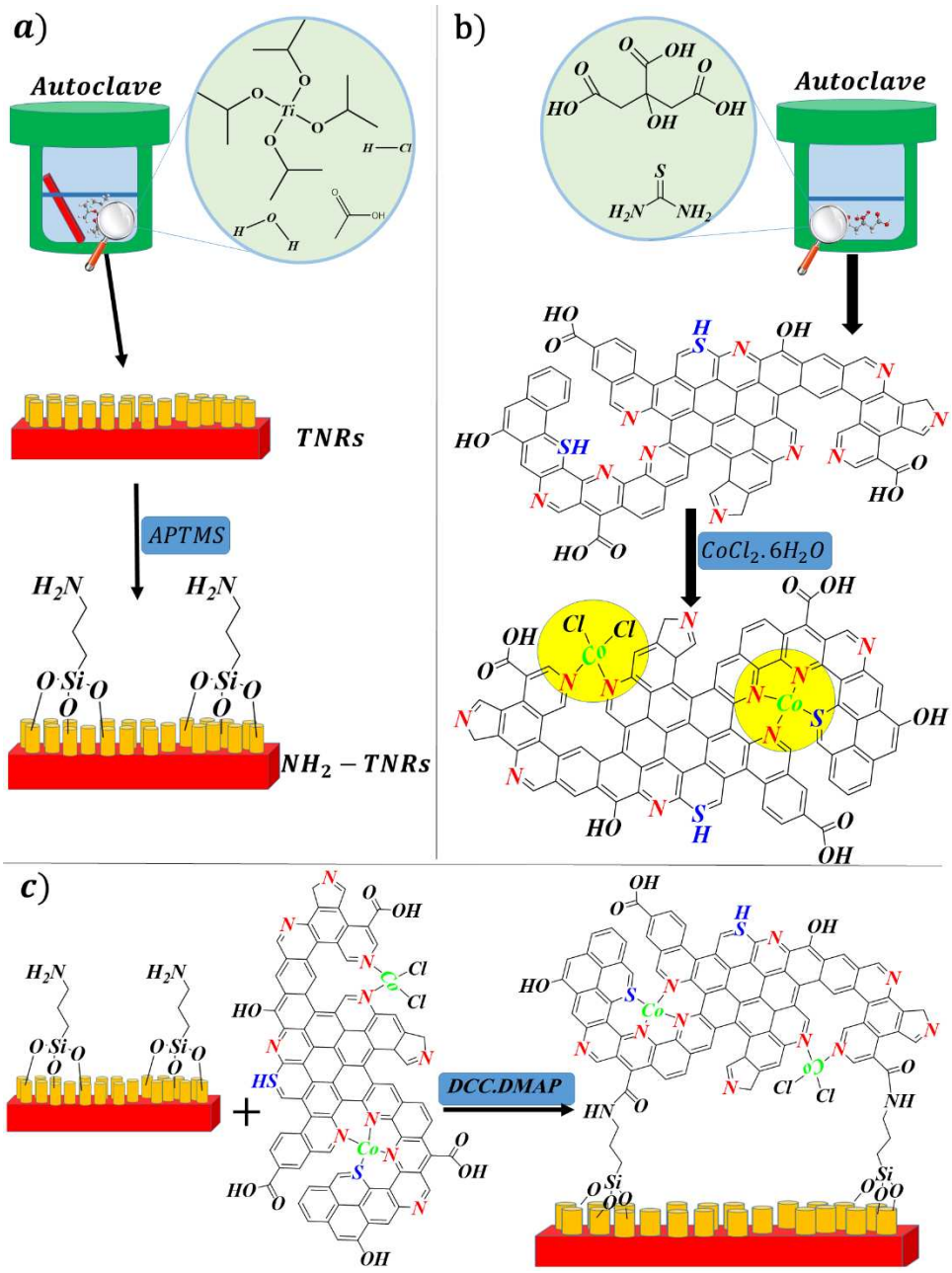

Scheme 1. Schematic representation of TiO_2 growth on FTO substrate a) S, N-GQD synthesis b) and modification of TiO_2 surface with Co-S, N-GQD c).

2.2 materials Characterization

Surface morphology and the electrode surface elemental analysis were evaluated with FESEM (Mira 2-XMU) and TEM (Philips). X-ray diffraction technique was used for the crystalline analysis of the products. After the preparation of KBr tablets, the synthesized

samples were characterized using the Bruker equinox 55. X-ray photoelectron spectroscopic (Bes Tec,10^{-10} mbar) analysis was used to investigate the surface composition of the synthesized sample. UV-visible (Perkin Elmer lambda 950) and photoluminescence analysis (Perkin Elmer) were also used to investigate the products' optical properties.

2.3 PEC measurements

Various photoelectrochemical analyzes were performed using a 3-electrode system with a glass cell with a quartz window. Ag/AgCl and platinum wire electrodes were used as the reference electrode and the counter electrode in the system. The phosphate buffer electrolyte with pH=6.8 was selected as the electrolyte, and we performed the tests without the use of any hole scavengers. The potentials obtained from the experimental data vs. Ag/AgCl electrode were converted to RHE using the following equation that obtained from Nernst equation:

(1) $E_{RHE} = E_{Ag/AgCl} + E^{0}_{Ag/AgCl} + 0.059pH$

Where E_{RHE} represents the potential versus RHE, $E_{Ag/AgCl}$ represents the potential vs. Ag/AgCl reference electrode that is practically obtained, $E^{0}_{Ag/AgCl}$ = 0.1976 V and the pH=6.8 which has been fixed at 6.8 with the help of phosphate buffer. 0.059 is obtained by placing constant values such as the universal gas constant, the Faraday constant, and the ambient temperature in Kelvins in the Nernst equation.

The following equation was used to calculate the photoconversion efficiency:

(2) photoconversion efficiency (%)= $\frac{J\left(\frac{mA}{cm^2}\right)[1.23-V_{app}]}{P\left(\frac{mW}{cm^2}\right)} \times 100$

Where J is the current density produced by the photoelectrode, V_{app} represent the potential applied, and P is the intensity of the incident light (100mW/cm^2).

Photoelectrochemical tests were performed using an AM 1.5G sunlight simulator and in 100 mW/cm^2 intensity. All the electrochemical measurements were conducted using a potentiostat (Ivium) with the Iviumsoft as software.

2.4- Computational analysis of electronic properties

In order to gain more insights into the electronic properties of the TNR-Co-S, N-GQD structure, we have done density functional theory (DFT) calculations[72,73]. The Vienna ab initio simulation package (VASP)[74,75]was applied by using plane-wave basis set and The generalized gradient approximation (GGA)[76]in the Perdew-Burke-Ernzerhof (PBE) [77]formalism for optimization with the projected-augmented wave (PAW)[78]method.

To get the correct band gap, GGA+U approximation [79] with effective U parameter of 8 for Ti 3d orbitals and Heyd-Scuseria-Ernzerhof (HSE0)[80]hybrid functional were used for TiO_2 and Co-S,N-GQD respectively.

3. Results and discussion

To use TiO_2 semiconductor in the visible region, it seems necessary to improve its optical and catalytic properties. Therefore, adopting a proper strategy to make these improvements is very important. Our primary strategy in this study was to use inexpensive materials and facile synthesis and preparation methods. Thus, we decided to use a single compound to improve the semiconductor's optical properties and be a suitable catalyst for the water oxidation reaction. The final choice was a combination of cobalt ions as the central metal and S, N doped GQD as the ligand for the metal ion. This complex alone is responsible for improving the optical and electron properties of the semiconductor. Then, due to the high solubility of these compounds in the aqueous electrolyte, we decided to use covalently

attached to the surface of the semiconductor. The purpose of nitrogen doping in the quantum dot structure was to form pyridine rings in the graphene structure. Pyridine structures can easily form coordinate bonds with transition metals due to the nitrogen electron pairs. Since the pyridine and cobalt structures together dramatically increase the rate of water oxidation reaction, it seemed that if the nitrogen-doped graphene quantum dot could act as a ligand for cobalt would have the same catalytic properties. On the other hand, doping sulfur in the quantum dot structure improves the visible light absorption of this compound. The bond of Co-S also reduces the charge transfer resistance of the electrolyte-electrode interface by increasing the electron transfer kinetics and, as a co-catalyst, leads to a significant increase in the output current efficiency of the photoelectrochemical cell. The strategy of using sulfur in the structure can be considered dual. On the one hand, by adding in the structure of GQD, it leads to an increase in the permissible transitions in the visible region and the absorption of visible light significantly improves, and on the other hand, by establishing a bond with cobalt (Co-S), it creates a structure that facilitates electron transfer[70]. The addition of sulfur can create more transitions in the visible region by increasing the electron levels, thus increasing the absorption of visible light by graphene quantum dot.

The schematic representation of synthesis processes was shown in scheme.1. The TiO_2 nanoarrays were hydrothermally grown on FTO substrate in step 1(scheme.1a). The S, N-graphene quantum dot synthesized in autoclave by hydrothermal method stirred with Co^{2+} ions to coordinated with heteroatoms in graphene quantum dots (scheme.1b) and the last step, the functional graphene quantum dots covalently attached on the surface of TiO_2 nanoarrays by DCC/DMAP functionalization. The combination of DCC and DMAP was used to activate the carboxylic acid groups in S, N-GQD to be easily attacked by amine groups on the surface of TiO_2, and the acidic group became an amide group. A graphene quantum dot is attached to the surface of the nanoarrays.

3.1 structure characterization

The rutile TiO_2 nanoarrays were synthesized on FTO substrate by using the mixed acid media[81]. In addition to simplicity, the method leads to the synthesis of highly ordered arrays and single-crystal TiO_2 semiconductor that provides a direct pathway for charge transport. The morphology was investigated by FESEM in cross-section and top of the surface view. Fig.1a and b observed the cross-section and top view of the nanoarrays, respectively. The nanorods' structural parameters, such as height and diameter, were controlled using the reaction time (4 hours)[38]. The nanorod arrays were grown on the surface with a length of about 2 µm and a diameter of less than 50 nm(30-40nm). In the synthesis method, vertical rods tend to form densely and close together perpendicular to the substrate surface. The proximity of the rods to each other provides a better pathway for transporting electrons from the semiconductor to the conductive substrate. However, scattering may occur less due to less light penetrating the side of the rods. In addition, adding acetic acid in the synthesis, resulting in a slight increase in the rods' diameter, leads to improving the photocurrent generated in the cell[81].

Fig.1c and d showed the top view pictures of the TiO_2 surface. Flower-like structures were formed on the nanorod structures, and photoelectrodes with dual morphology were synthesized. Flower-like nanostructure helps increase light scattering and, thus, better electrode efficiency. These structures compensate for the reduction in light scattering due to the formation of the dense structure of the nanorods. In fig.1e and f, the up view surface images are related to surface-modified nanoarrays with S, N-GQD. As shown in the figure with the arrow, very tiny particles of quantum dots are placed on the flower-like structures. However, due to the small size of the quantum dots, it is not easy to detect them by FESEM analysis.

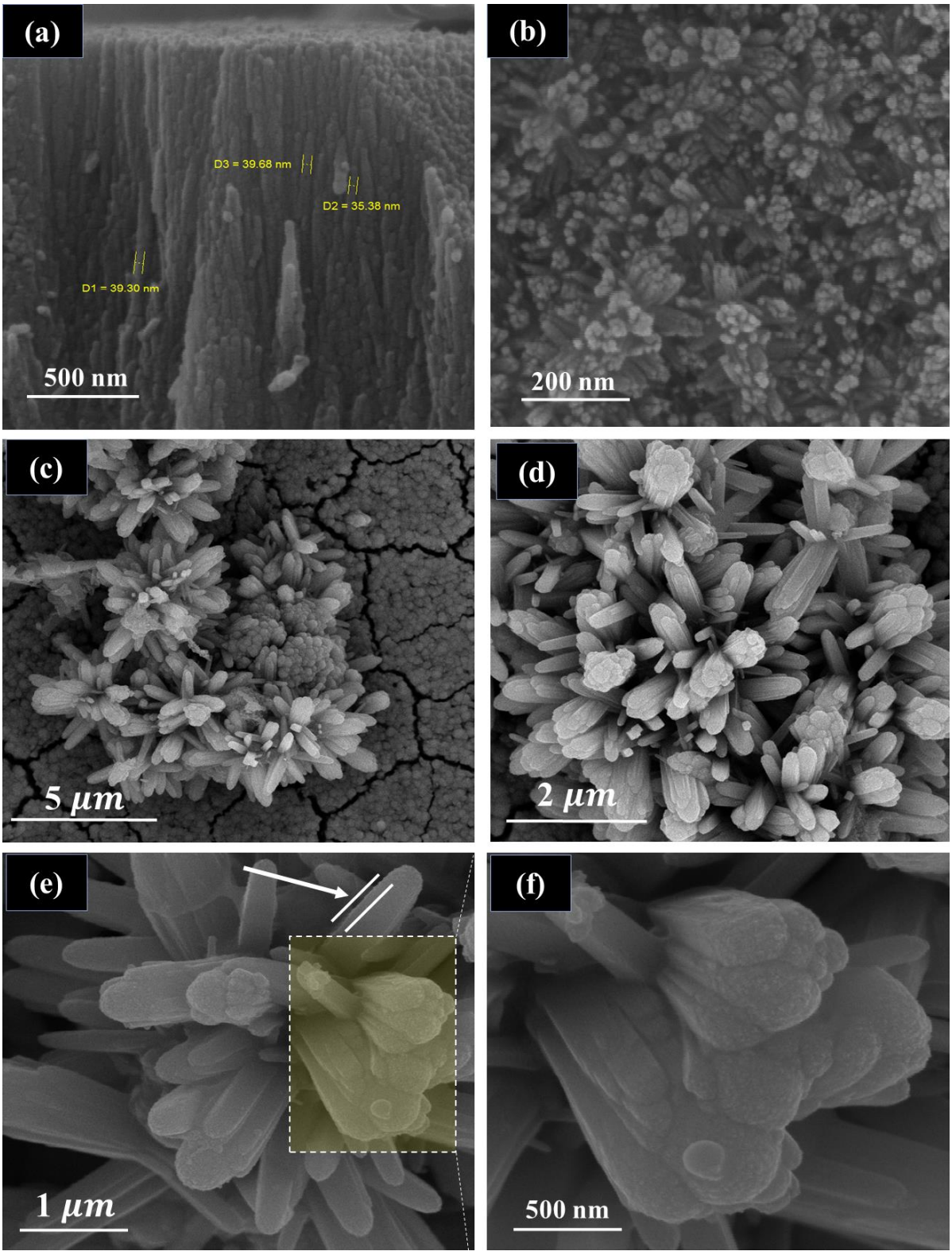

Figure 1- FESEM images of TiO_2 nanoarrays in cross-section (a and b), top view (c and d), and TiO_2 arrays modified with Co-S, N-GQD (e and f) in various magnification.

TEM images were used to more accurately study the structure and morphology of the synthesized quantum dot. As shown in Fig.2a and b, quantum dots are synthesized as spherical (or hexagonal) shapes. These quantum dots appear to be between 5 and 10 nanometers in diameter. However, their structure has aggregated in these images because the quantum dots have been dispersed in ethanol. The aggregation of these particles has made it a bit difficult to determine their exact size. Unassembled structures appear to be less than 10 nm in diameter. The TEM images of TNR-Co-S,N-GQD are also shown in Fig.2 c and d. As can be seen, the quantum dots are well placed on the surface of the semiconductor.

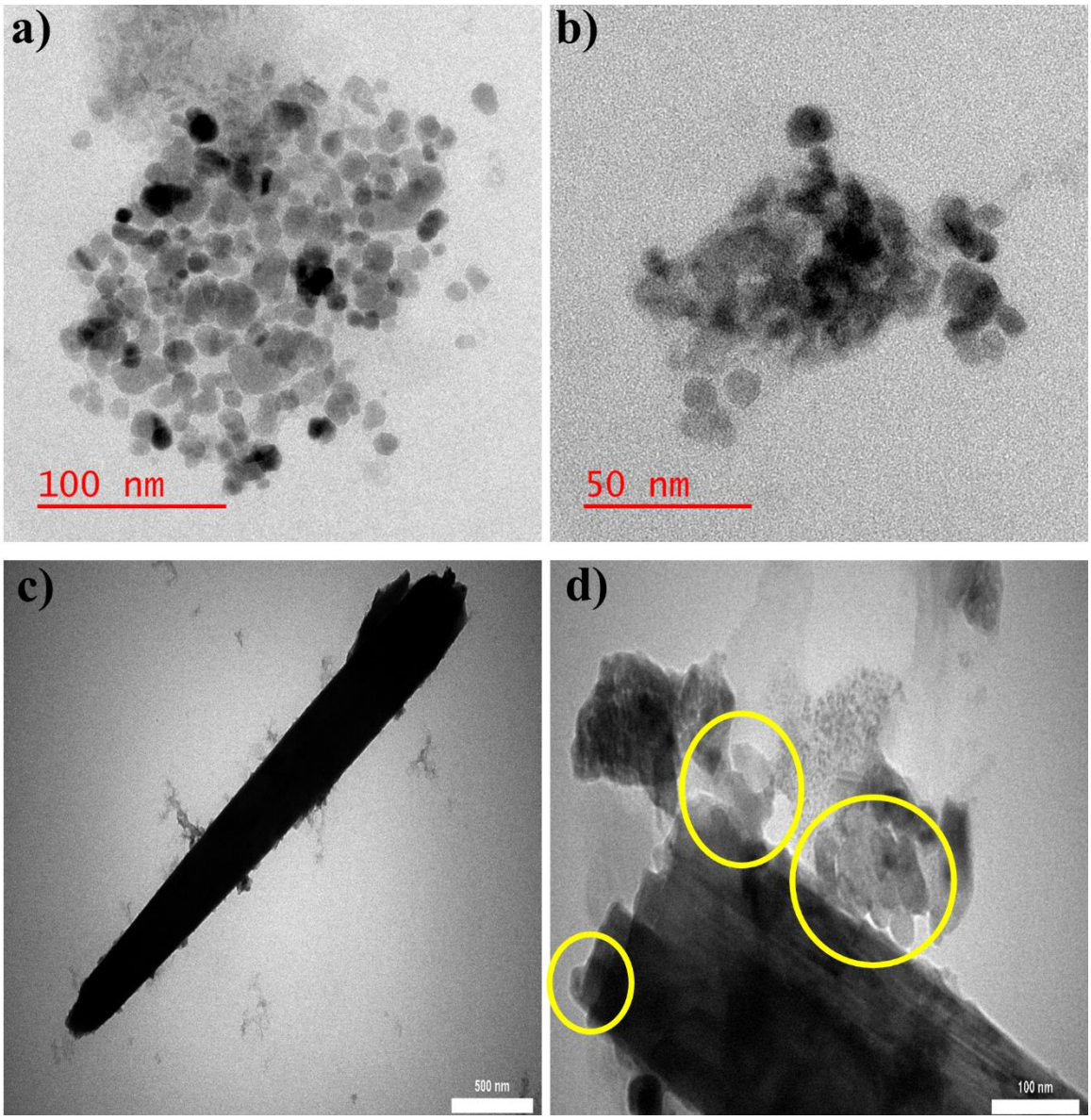

Figure 2- TEM image of S, N-GQD a), b) and TNR-Co-S,N-GQD c), d) in various magnification

Fig3 shows the energy-dispersive spectroscopy (EDX) of the TNR-Co-S, N-GQD electrode surface. By the analysis, the element percentages of the photoelectrode surface were obtained. As expected, titanium, carbon, and oxygen are the main constituents of the photoelectrode. It is found that the percentage of N and S in the structure of S, N-GQD is close to each other, and the amount of Co is close to half a percent. As expected, cobalt was deposited on the photoelectrode surface and did not dissolve inside the electrolyte.

On the other hand, the presence of sulfur and nitrogen on the electrode surface indicates the proper stability of the quantum dot on the semiconductor surface against dissolution in the electrolyte. Data from other analyzes, such as XPS, suggest that the percentage of nitrogen in the quantum dot structure is higher than that of sulfur. In contrast, EDX analysis has shown the percentage of these two elements close to each other. Therefore, we can infer that sulfur tends to be on the outer surface of the quantum dot and thus play a positive effect on the visible light absorption of the quantum dot.

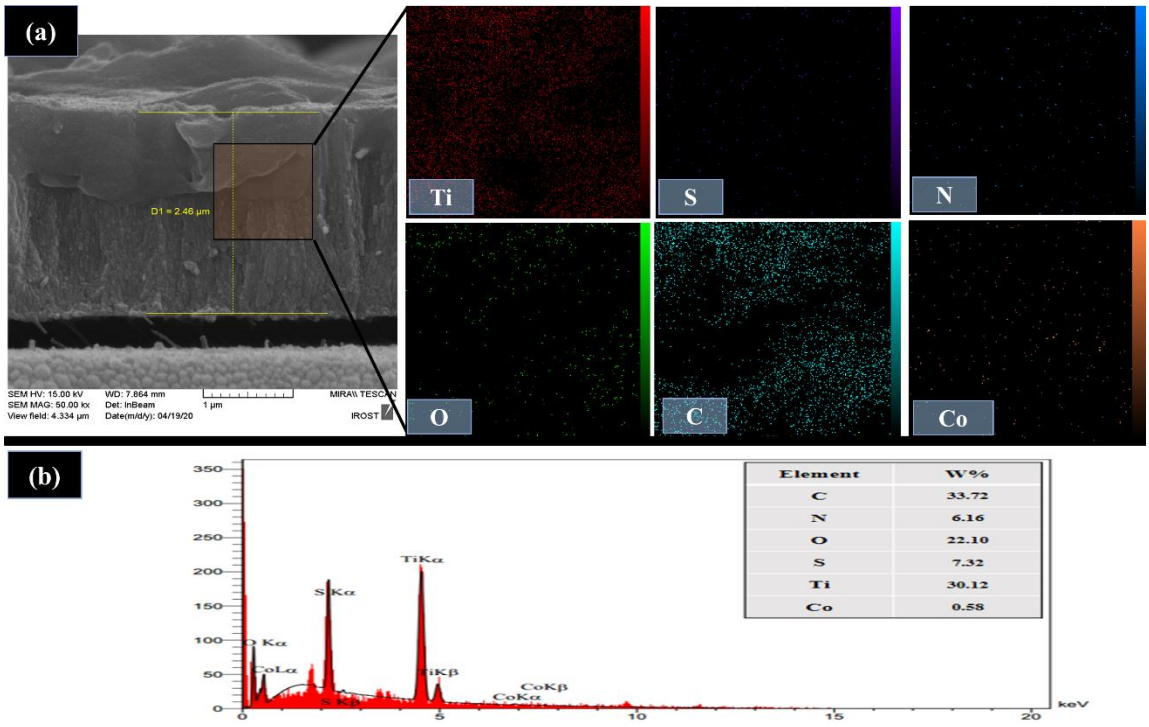

Figure 3- a) FESEM and Ti, S, N, O, C and Co mapping of TNR-Co-S, N-GQD photoelectrode and b)EDX analysis of TNR-Co-S, N-GQD

Fig.4 (a-b) shows the XRD patterns of TNRs on FTO substrate, S, N-GQD, and Co-S, N-GQD, respectively. In the spectrum in fig.4a, the rutile TiO_2 phase's diffraction pattern is shown along with the FTO substrate's peaks. The six peaks observed in 2θ values of 27.5°, 36.3°, 41.3°, 54.4°, 62.8°, and 65.2° are all related to the structure of the rutile. The plane attributed of peaks is shown in Fig.4a. The most significant tetragonal rutile phase peaks, including planes (101) and (002), are specified in the pattern (JCPDS file no. 21-1276)[37].

The peak intensity of 002 indicates that the TiO_2 nanostructures are well synthesized in one direction (001). Because graphene quantum dot has an amorphous structure, the peaks in this compound's diffraction pattern are not sharp (fig.4b). The broad peak around 23° corresponds to the 002 planes of graphitic carbon[49]. Fig.4b shows the diffraction pattern for [Co-S, N-GQD]. The graphitic carbon peak has shifted slightly to a lower angle (21), indicating an increase in the distance of the layer. The shifting may be due to the placement of Cobalt metal between the plates. On the other hand, the diffraction pattern of S, N-GQD is not the same as before, which indicates that the structure of the compound has undergone significant changes.

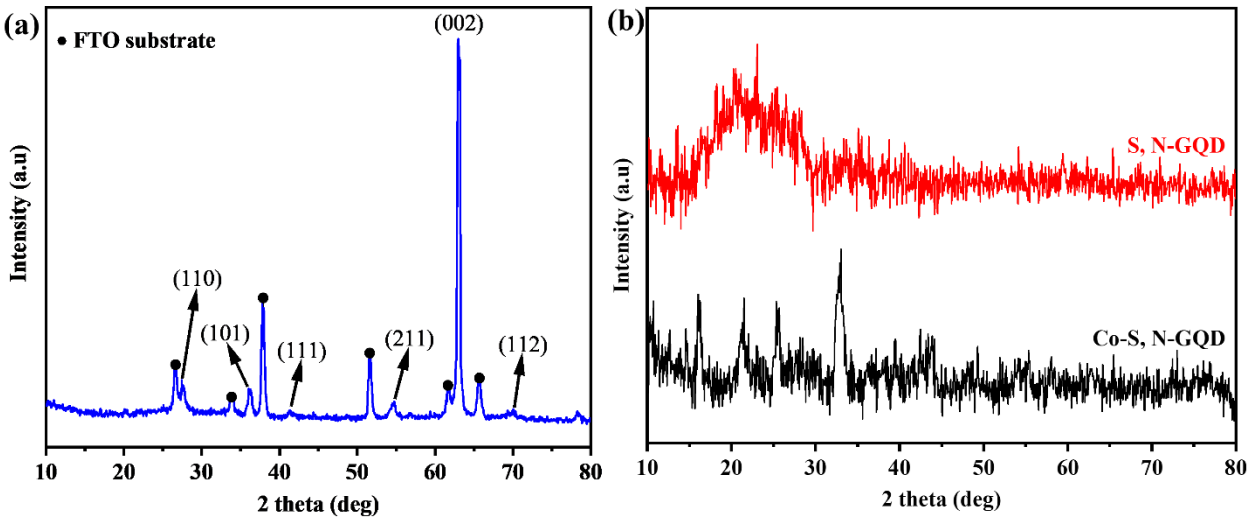

Figure 4-XRD pattern of a) TiO_2 nanorod arrays on FTO substrate and b) S, N-GQD and Co-S, N-GQD

XPS analysis was used to investigate the synthesized surface composition further and confirm the elements' chemical states. Fig.5a shows the survey spectrum of [Co-S, N-GQD] with peaks for C, S, N, Co, Cl, and O. As shown in the spectrum, the elements carbon, nitrogen, and oxygen are the main constituents of graphene quantum dot. Sulfur and cobalt have lower peak intensities than other elements due to their lower amount in the final structure of the quantum dot. In fig.5b, the high-resolution peak corresponding to C 1s is deconvoluted in five peaks. The C-C and C=C bond appear in region 284.6 eV related to C in graphene structure[82]. The peak of C-N and C-S bonds in region 285.9 eV[83],

the peak of region 286.8 eV corresponds to the bond of C-OH[84], the peak of region 287.9 eV belongs to the C=O bond, and the peak of region 289.5 eV belongs to the COOH group[82,85]. As shown in the spectrum, due to the high percentage of heteroatom doped in the structure, the highest peak intensity is related to the carbon-nitrogen and carbon-sulfur bonds. The intensity of peaks at the edge of the sheet, including the COOH, C=O, and C-OH peaks, constitutes a significant percentage of the peak level. These peaks indicate that the edges of the graphene sheet are often edge-functionalized.

According to Fig.5c, the deconvoluted spectrum of N 1S can be divided into four peaks. Peaks of pyridinic, pyrrolic, and graphitic N in 398.8 eV, 401.5 eV, and 402.3 eV have also appeared in this spectrum[86]. The presence of a peak in 398.5 eV indicates the formation of the bond between Cobalt and Nitrogen, which confirms the coordination of metal-nitrogen in the structure [87,88]. The spectrum shows that the highest percentage of nitrogen is related to pyridine nitrogen. Hence, the possibility of a bond between cobalt and nitrogen increases.

In order to study the synthesized structure in more detail, high-resolution XP spectrum of O 1s was also studied. As shown in Fig5.d, the O 1s peak was divided into two peaks. The first peak, which appears in area 532.2 eV, is related to the C=O bond. The peak in 533.4 eV also corresponds to the C-O bond[89–92]. As shown in the fig5.d, the double bond forms a higher percentage (about 70%) of the oxygen bond and the single bond is lower(about 30%.

Fig.5e shows the deconvoluted spectrum of S 2p that can be divided into four peaks. S-C and S =C bonds appeared in 162.8 eV, 163.7 eV, and S=O bonds appear in 165 eV [93]. The presence of another peak in area 161.5 is also related to the bond between Co and S that is Another evidence of the bonding between cobalt and heteroatoms in the structure of S, N-GQD [93,94].

Fig.5f shows the high-resolution spectrum of Co 2p. The peak of area 781.3 is related to the presence of Co^{2+} in the composition [93,95]. Given that Co's peak appeared in the area

of 781.3 eV, it can infer that the peak is related to Co^{2+} in the Co-N bond [88]. It seems more than the region corresponding to the cobalt oxide peak(779-780). Metallic cobalt also appears in area 779 eV. The formation of cobalt and graphene quantum dot complexes and the construction of cobalt-nitrogen bonds positively affect electron transport and catalytic properties in the photoelectrochemical cell.

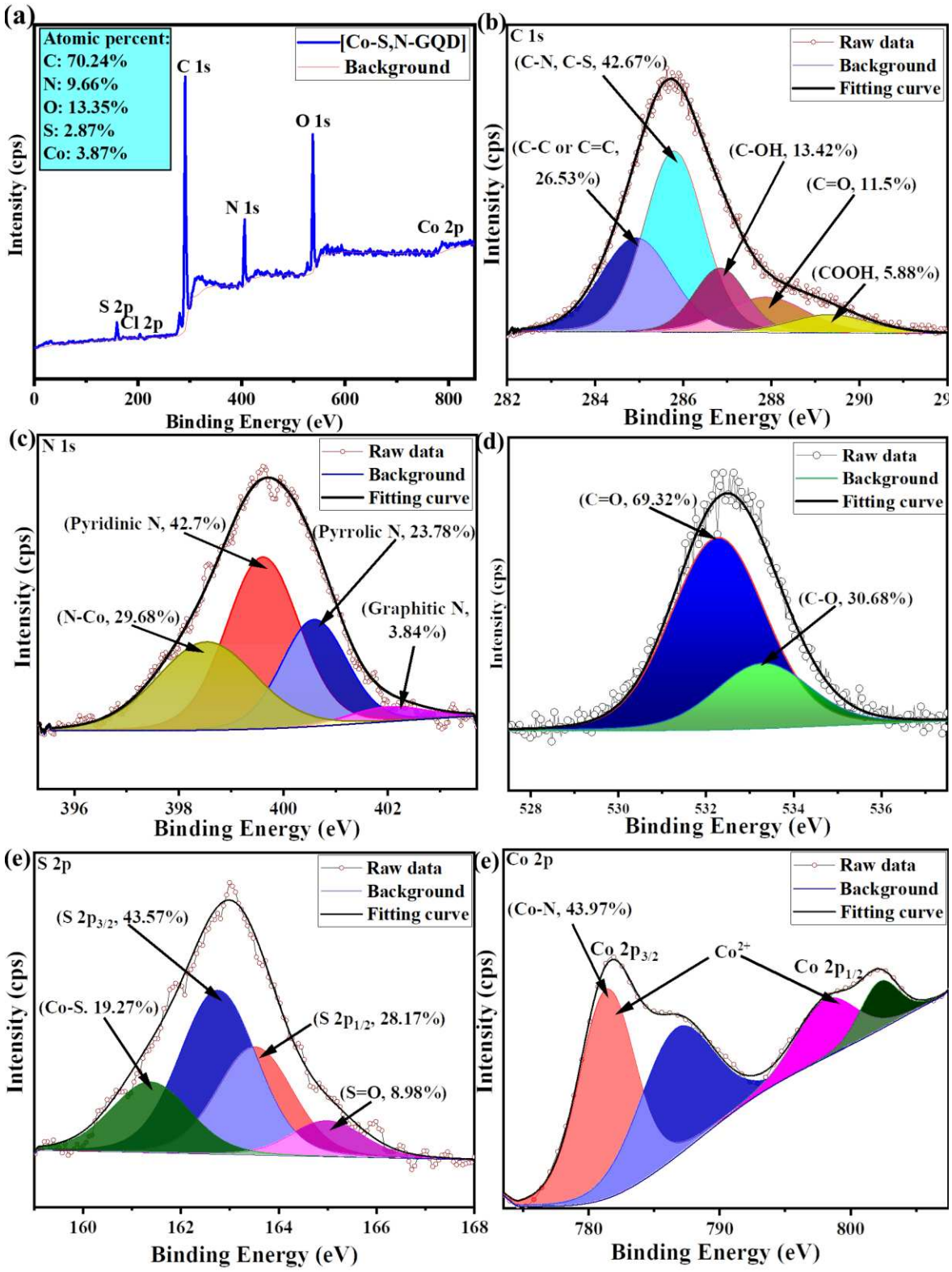

Figure 5- a) XPS survey of Co-S, N-GQD, and high-resolution XPS of b) C 1s c) N 1s d) O 1s e) S 2p and f) Co 2p.

FTIR analysis was used to investigate further the structure and functionalization of the compounds (fig6). In TNR spectra, the peaks appearing in the pre-1000 cm^{-1} region are related to the tensile vibrations of TiO_2[60,61]. In NH_2-TNR spectra, which deals with amino silane-modified TiO_2, the peak in area 2931 cm^{-1} is related to the C-H bending vibration. The 1630 cm^{-1} peak is associated with the NH_2 group of aminopropyl trimethoxysilane[62]. In the S, N-GQD spectrum, the peak appearing in 1717 cm^{-1} is related to the acidic carbonyl bonds present in the structure[50,63]. The peaks in areas 1575 cm^{-1} and 1413 cm^{-1} are related to the tensile vibrations of C-C and C-N[50]. In the final spectrum for compound TNR-Co-S, N-GQD, graphene quantum dot peaks cover the peaks related to TiO_2. However, the peak of carboxylic acid, which appeared in 1717 cm^{-1}, was shifted to 1627 cm^{-1}, indicating carboxylic group conversion to amide groups and GQD attachment to the surface of functionalized TiO_2.

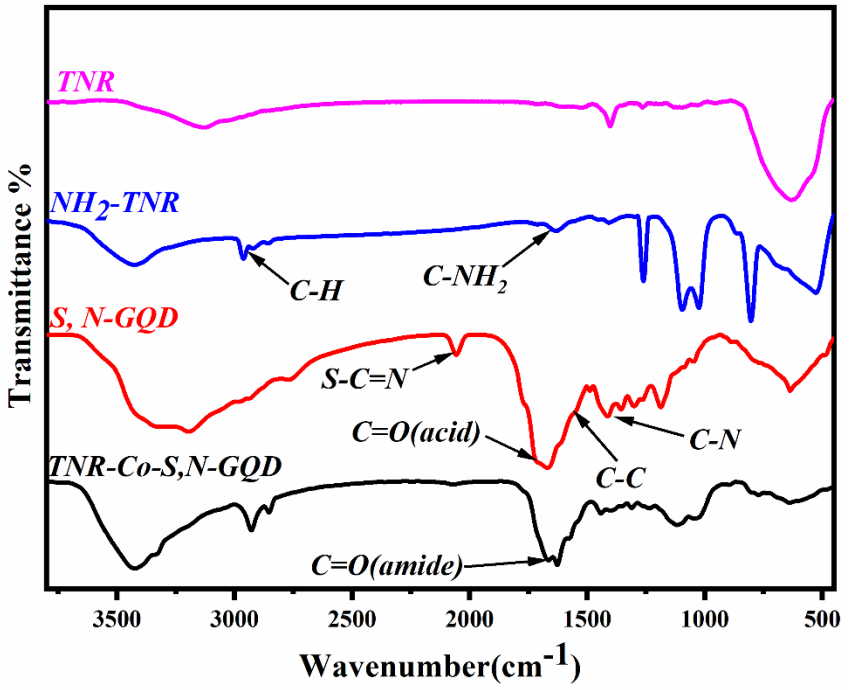

Figure 6- FTIR spectra of TNR, NH_2-TNR, S, N-GQD and TNR-Co-S, N-GQD

UV-visible spectroscopy was used to investigate the effect of doping heteroatoms on the structure of GQD on its optical properties. As shown in Fig.7a, the presence of four additional peaks in the visible area has caused a difference in the optical absorption behavior of these two compounds. Both spectra recorded sharp peaks in the 334 nm region. Due to the presence of the carbonyl group in the structures of both compounds, the peak is related to the n→π* transition of the bond. In addition to this peak, S, N-GQD has shown visible light absorption in 402 nm, 550 nm, 591 nm, and 626 nm. These absorptions indicate a much better performance of the compound in visible light absorption. The four added peaks in the S, N-GQD spectrum are related to the addition of sulfur to the structure and bonds such as C=S and S=O. The addition of these bonds to the structure of GQD has led to the addition of n→π* and π→π* transitions of the functional groups and has led to the absorption of more appropriate light in this region. The Tauc plot of [S, N-GQD] is shown in the inset of Fig.7a inset. Using the following equation, the optical band gap of S, N-GQD was calculated:

$$(3)\alpha h\nu = A_0\left(h\nu - E_g\right)^n$$

Where α indicates the absorption coefficient, A_0 is a proportionality constant, n=1/2 or 3/2 for direct allowed transition and indirect allowed transition respectively, E_g indicates the band Gap material, and $h\nu$ indicates the corresponding photon energy. According to the Tauc plot, we calculated the material's optical bandgap to be 2.3 eV that is less than the TiO_2 band gap (3.04 eV), and has made the two together perform well use photoelectrochemical cells.

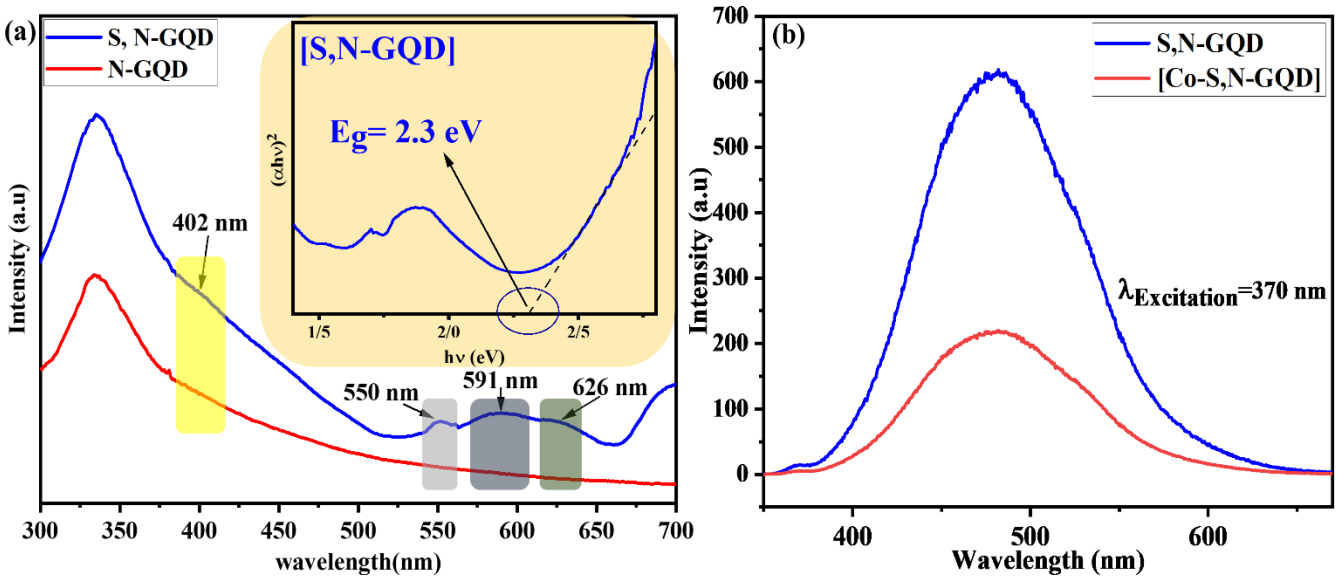

Figure 7- a) UV-visible spectrum of S, N-GQD and N-GQD and, Tauc plot of S,-N-GQD inset and b) PL spectrum of S, N-GQD and Co-S, N-GQD.

Photoluminescence spectroscopy is used in the field of photoelectrochemical reactions to study the behavior of charge carriers. The spectroscopy is based on the transfer behaviors and lifetime of electrons and holes. Specifically, lower photoluminescence intensities indicate the longer lifetime of electrons and holes, resulting in less charge recombination[96]. Fig.7b shows the photoluminescence spectrum of the S, N-GQD, and [Co-S, N-GQD]. The S, N-GQD spectrum shows a peak emission at 480 wavelengths. However, when Co^{2+} ions were added to the quantum dot by 2% by weight, the emission intensity dropped dramatically. This intensity initially indicates an excellent interaction of quantum dot with Co^{2+}. Quantum dots have also been used to build a selective sensor to detect cobalt ions[97]. By studying the spectrum, it is concluded that the coordination bond between cobalt ions and quantum dot will increase the lifetime of charge carriers and reduce their recombination, which will improve the photoelectrochemical performance of the final compound.

To investigate the effect of S, N-GQDs adding on light absorption properties of TiO_2 nanoarrays, diffuse reflectance spectra of both samples were analyzed. Fig.8a and b show these two spectra with the corresponding Tauc plots for each sample. As it turns out, TiO_2

does not offer much absorption in the visible region. This compound has a good absorption in the UV, and by entering the visible area, its intensity of absorption peak is gradually reduced. The bandgap of this compound was estimated at 3.04 (rutile). Examining the spectrum of the mixture of TiO_2 and S, N-GQDs, we can see that the absorption spectrum of the region before 400 nm has affected the absorption behavior of TiO_2, and the bandgap has been reduced to 2.75 eV. This spectrum shows a combination of TiO_2 and quantum dot spectra. Proper absorption in the UV region, which is related to TiO_2, and improved absorption in the range of 350 to 600 nm, which is achieved due to the addition of quantum dot to the structure. This improvement has led to the semiconductor being more sensitive to visible light. Therefore, we can expect an improvement in the photoelectrochemical performance of the semiconductor due to the improved light-harvesting efficiency.

Using PL analysis, the structure of the edges of the GQD sheets can be understood[98]. The edges have a zigzag, armchair, or edge-functionalized structure. The presence of emission peaks in 405 nm, 441 nm, 480 nm, and 521 nm corresponds to the zigzag-edge, armchair-edge, carboxylic acid-functionalized edge, and carbonyl-functionalized edge, respectively. To understand the exact structure of GQDs, the peak appearing in the PL spectrum was divided into its constituent peaks. As shown in Figure 8c, the area below the zigzag edge peak, which appears at 405 nm, accounts for a small percentage of the total peak, indicating that most of the edges of the quantum dot are armchair. As expected, a high percentage of graphene sheet edges are functionalized by the carboxyl and carbonyl groups because of the intensity of the peaks that appear in the region of 480 and 521 nm, were correspond to the carboxyl and carbonyl edges, respectively. Table 1 shows the exact percentage of edge formation using deconvolution of the PL spectra emission peak at the excitation wavelength of 360 nm.

Table 1-percentage of edge structure of S, N-GQD sheets based on PL spectrum

Edge structure	peak area (nm)	percentage (%)

Zigzag-edge	405	3.55
Armchair-edge	441	32.02
Carboxyl functionalized-edge	480	40.03
Carbonyl functionalized-edge	521	24.41

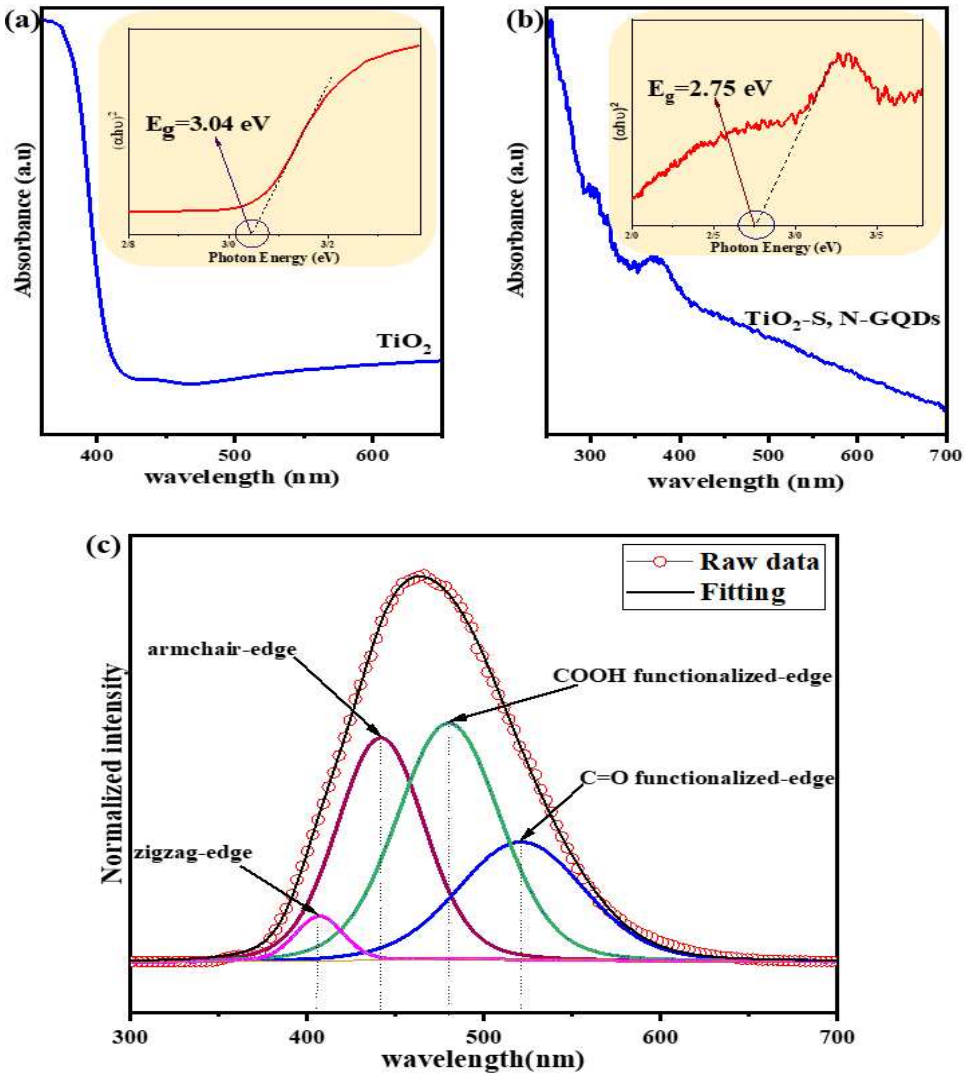

Figure 8-UV-visible diffuse reflectance spectrum and Tauc plot of a) TiO_2 nanoarrays and b) TiO_2-S, N-GQDs. c) PL spectra (excited by 360 nm laser) of S, N-GQD at room temperature and its deconvolution to basic peaks.

N_2 adsorption-desorption measurements were used to evaluate the porosity and BET surface area of S,N-GQD and Co-S,N-GQD. Fig9.a shows diagram of N_2 adsorption-desorption for these two structures. Table 2 shows the parameters related to the porosity and the size of the pore obtained from this diagram. As it turns out, the addition of cobalt to the structure has led to an increase in the surface area of the structure from 4.78 m^2/g to 15.58 m^2/g. Also, the average pore diameter has decreased from 45.82 nm to 19.67 nm.

Thermogravimetric analysis (TGA) was used to investigate the temperature behavior of Co-S,N-GQD. Fig9.b shows the TGA diagram of this compound. As it turns out, the sample goes through a weight loss step from 25℃ to 169℃. During this step, the sample loses 7.74% of his weight. Loss of less than 10% by weight below 200°C may indicate the removal of physically adsorbed water. In the next stage, the sample loses 6.2% of its weight from 169 ℃ to 253℃, which can also be related to nitrile oligomerization or the exit of other gaseous products. After this stage, the intensity of weight loss increases and up to 600℃, another 33% of the sample mass is lost.

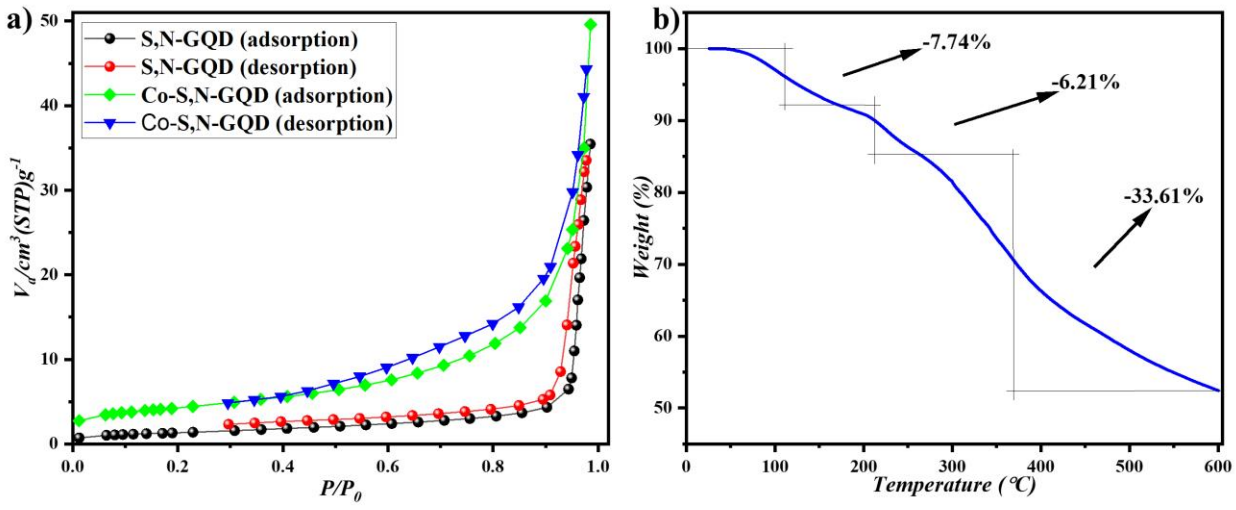

Figure 9- a) N_2 adsorption-desorption diagram of the S,N-GQD and Co-S,N-GQD. b) TGA curve of Co-S,N-GQD in N_2 atmosphere with heating rate of 10°/min

Table 2-BET parameters of S,N-GQD and Co-S,N-GQD

	$a_{s,BET}$ (m^2/g)	average pore diameter (nm)	v_m(cm^3/g)
S,N-GQD	4.78	45.82	1.09
Co-S,N-GQD	15.58	19.67	3.58

3.3 DFT calculations

Fig.9 shows the structures and their corresponding density of states (DOS) of the TNR-Co-S, N-GQD. The structure of rutile TiO_2 (001) and its DOS are shown in Fig.9a. According to the DOS, band gap energy of TiO_2 is 2.99 eV which agrees well with the UV spectrum band gap result of 3.04 eV. From Fig.9a, it is found that while the conduction band (CB) of TiO_2 structure is dominated by d orbitals of Ti atoms with energy of 2.971eV, the VB is mainly occupied by p orbitals of O atoms (-0.022 eV). The structure of Co-S, N-GQD with its DOS is illustrated in Fig.9b. In order to mimic the experimental observations, we constructed GQD with armchair edge based on the Lerf-Klinowski [99] model suggesting that the GO terminates with oxygen containing functional groups of hydroxyl and carboxyl. The DOS of Co-S, N-GQD, Fig.9b, shows the energy band gap of 2.36 eV, where its LUMO and HOMO energies are 5.102 and 2.745 eV, respectively. The greater LUMO energy of Co-S, N-GQD (5.102 eV) than CB of TiO_2 (2.971 eV) confirms the photoexcited electron transfer from the excited states of GQD complex to the CB of TiO_2, which is also seen in other studies[100,101].

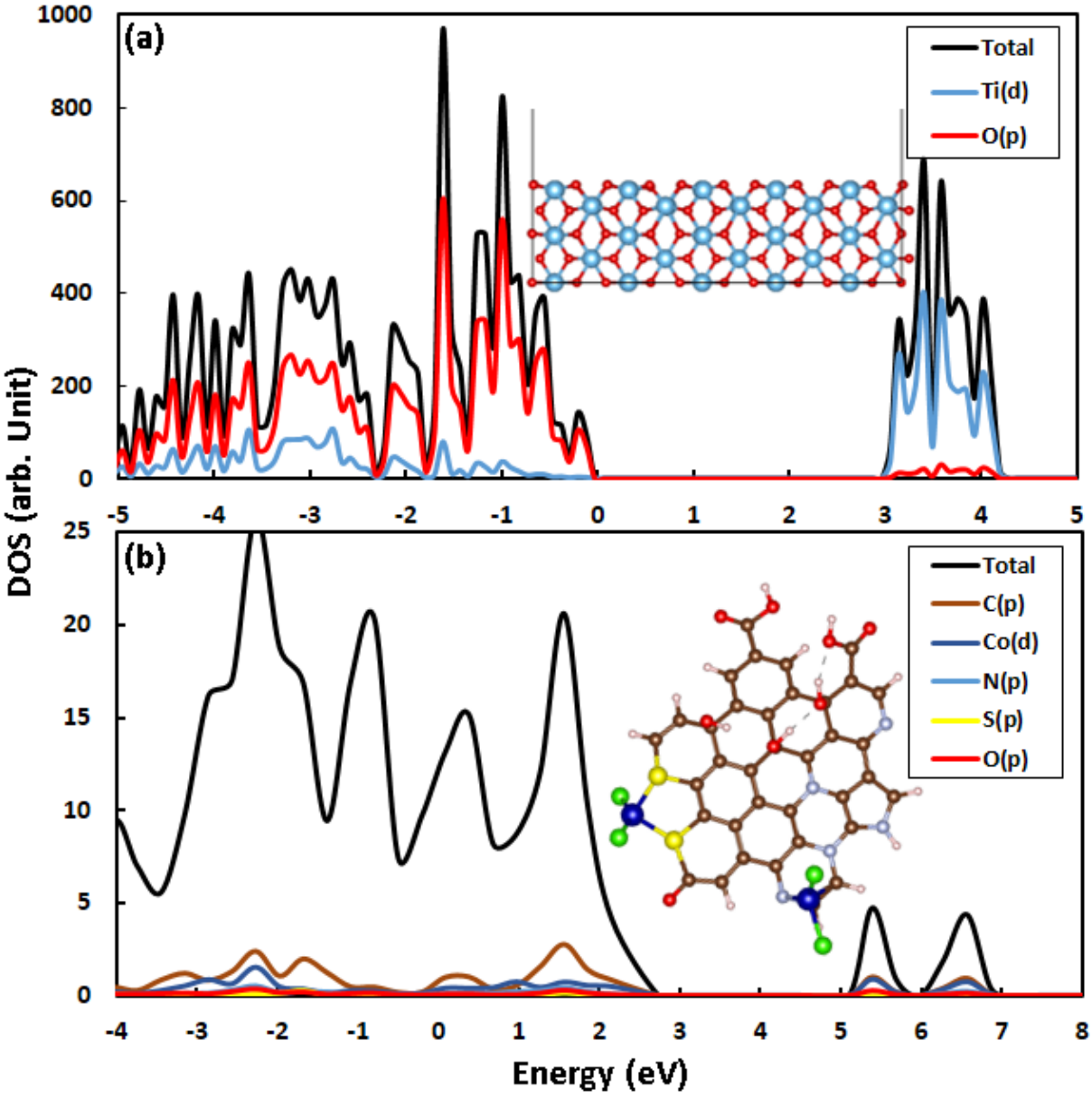

Figure 9- The structure and DOS of a) TiO_2 (001), b) Co-S, N GQD.

3.2 PEC performance

The photoelectrochemical performance of the synthesized materials was investigated in the form of various electrochemical analyses. These tests, which were performed on 3-electrode cells, used phosphate buffer with a pH of 6.8 as the electrolyte, and all of the tests

were measured at 100 mW / cm^2. The first step was to study the linear sweep voltammetry test, in which the current behavior of the cell was investigated based on potential. To better express the optical behavior of photoelectrodes, measurements were performed in both dark and light conditions. As shown in Fig.11a, no current was observed in the dark for TNR-S,N-GQD. In TNR photoelectrode, the current density is 0.477 mA/cm^2. The current density increases to 0.681 mA/cm^2 when S, N-$GQD_{0.4}$ sensitizes the electrode surface. After modifying the photoelectrode's surface with [Co-S, N-GQD], the photocurrent density increases to 1.141 mA/cm^2, which is about 2.5 times compared to unmodified nanoarrays. In Fig11.b, the photoconversion efficiencies of each electrode were reported. As it turns out, TNR-Co-S,N-GQD has the highest return with a efficiency of 0.577% at a potential of 0.68V vs RHE. Different amounts of S,N-GQD were also used to investigate the quantitative effect of quantum dot on cell efficiency. As shown in Fig.11b, the highest returns were related to TNR-S,N-$GQD_{0.2}$. Fig.11c shows the chronoamperometry test for different electrodes at 1.23 V regarding light on and off.

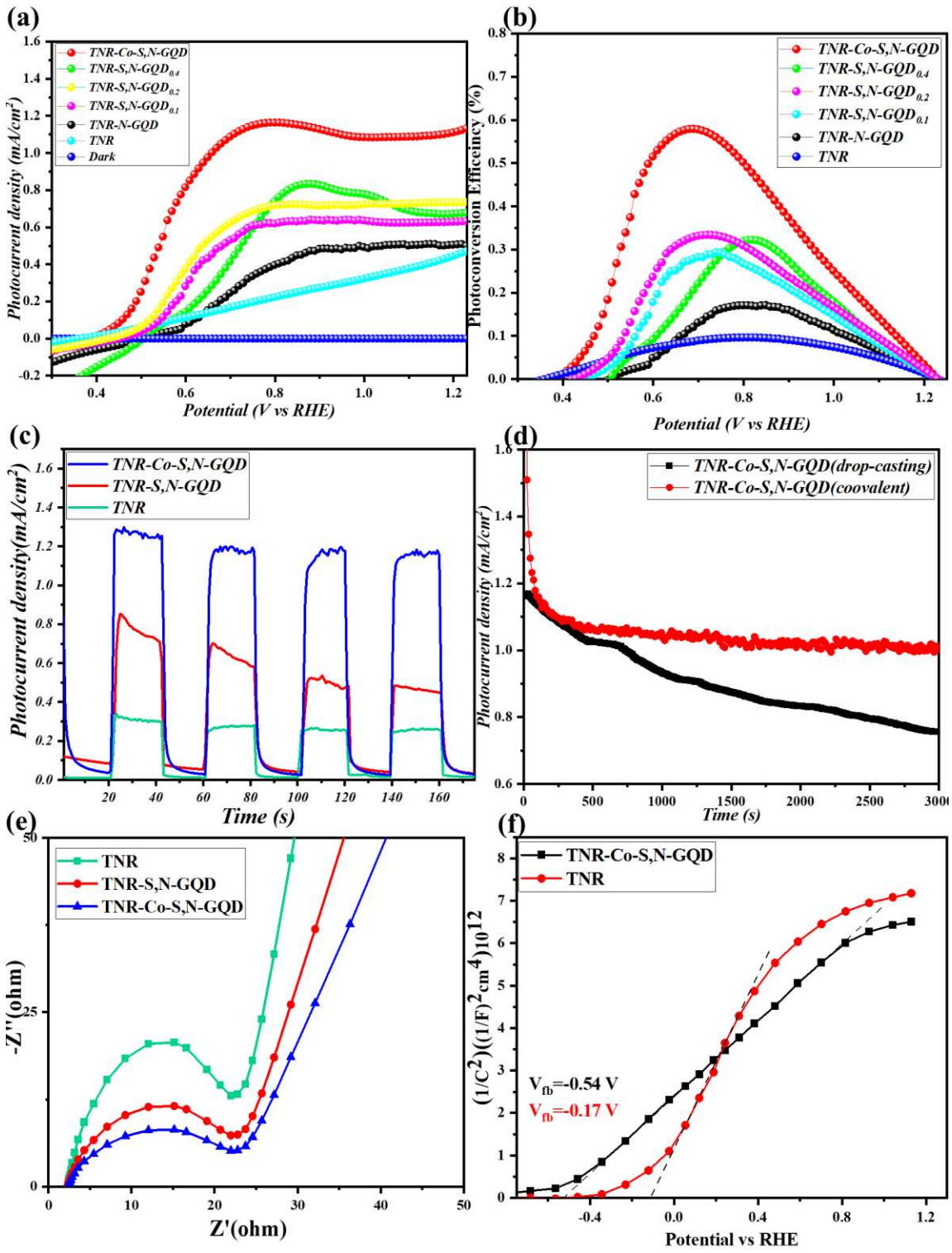

Figure11- a) LSV measurements, b) Chronoamperometric measurements, and c) impedance spectroscopy of TNR, TNR-S, N-GQD, and TNR-Co-S, N-GQD. d) Mott-Schottky analysis of TNR and TNR-Co-S, N-GQD in the range of -0.4 to 1.25 V vs. RHE.

To evaluate the stability of the fabricated electrode, chronoamprometry test was performed for a long time (fig11.d). In this test, a comparison was made between covalently modified surface photoelectrode and non-covalent photoelectrode coated on TNRs. As shown in the fig11.d, the covalently modified electrode does not show a significant reduction in current. In contrast, the non-covalent electrode significantly reduces the current over time.

In fig.11e, we investigate the transfer characteristics of charge carriers using electrochemical impedance spectroscopy. With the analysis help, the charge transport resistance at the electrolyte interface and the photoelectrode were investigated. In this part, the photoelectrodes of TNRs and TNR modified with S, N-GQD (TNR-S, N-GQD), and TNR modified by [Co-S, N-GQD] (TNR-Co-S, N-GQD) were analyzed under simulated light and one sun intensity and at the 1.23 V vs.RHE. As shown in the diagram, the TNR-Co-S, N-GQD photoelectrode has a lower charge transfer resistance. The charge carriers pass through the interface between the electrolyte and the photoelectrode at the modified electrode faster than the unmodified nanoarrays, increasing the photocurrent. This analysis is entirely consistent with the current-voltage analysis. Interestingly, the presence of cobalt on the surface of the photoelectrode, while interacting with pyridines in the quantum dot structure, significantly increased electron transfer from the interface between the electrode and the electrolyte.

Fig11.f deals with the mott-Schottky (M-S) analysis of TNR and [Co-S, N-GQD] photoelectrodes. The analysis was used to determine the density of charge carriers and the potential of the flat band. Using the M-S equation:

$$(4)\ \frac{1}{C^2} = \left(\frac{2}{e\varepsilon\varepsilon_0 N_D}\right)\left[(V - V_{FB}) - \frac{kT}{e}\right]$$

which N_d represents the charge carriers concentration, C represents the capacitance of space charge region, V_{FB} represents the flat band potential, ε_0 represents the vacuum permeability, ε represents the dielectric constant (here it refers to the TiO_2 layer, which is

considered to be 55), V represents the applied potential, T represents the ambient temperature, k represents the constant Boltzmann and e represent the charge of an electron. According to the equation, from the slope and the extrapolation of the diagram, the values of the charge carrier concentration and the flat band potential can be obtained, respectively.

On the other hand, the slope of the diagram indicates the type of semiconductor. As shown in the fig.10d, the positive slope of the curves indicates the n-type semiconductor. Photoelectrode of [Co-S, N-GQD] shows a lower slope than TNR, indicating a higher charge density and a more extensive discharge layer. The flat band potential can be determined from the diagram's intercept specified in the fig.10d. As shown in the fig.10d, the flat band potentials of TNR and [Co-S, N-GQD] are estimated to be -0.17 V and -0.54 V, respectively.

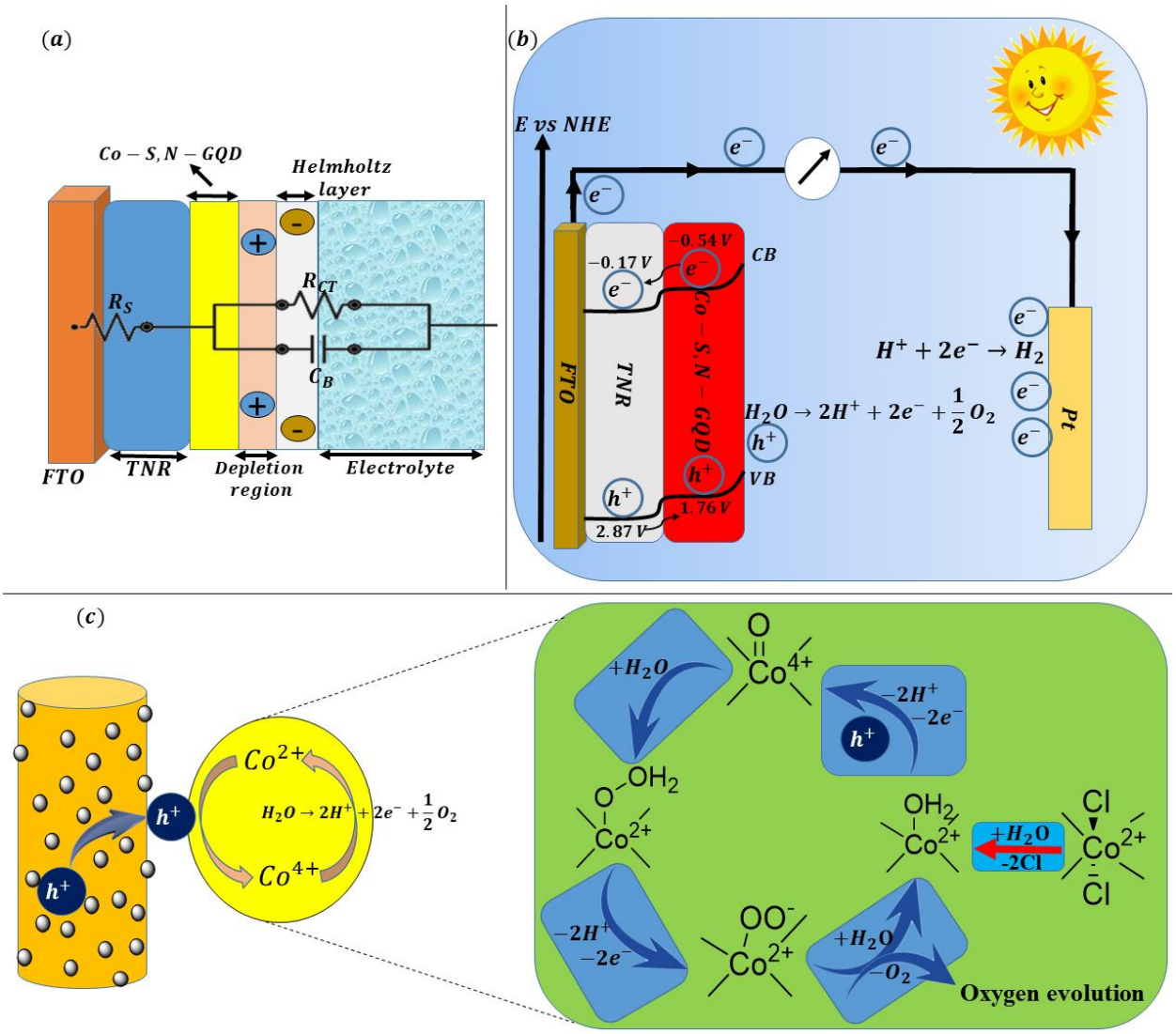

Scheme2- a) equivalent circuit diagram of photoelectrode through EIS, b) schematic diagram of charge carrier separation and their injections mechanism and c) proposed mechanism of water oxidation catalysis with Co^{2+} and nitrogen bond by Co^{4+} as an intermediate.

Scheme.2a schematically shows the equivalent circuit for the modified photoelectrode. The results of impedance analysis and fitting the data on the interfaces, exact numbers related to the different resistances in the circuit were obtained. In the circuit, the R_S corresponds to the photoelectrode's resistance of the substrate. The R_{CT} corresponds to the resistance of the charge transfer between the photoelectrode and the electrolyte interface, which is related to the transport of electrons from the quantum dot to semiconductor and from

semiconductor to the substrate. Table 3 represents the R_S and R_{CT} and C bulk values for the three electrodes TNR, TNR-S, N-GQD, and TNR-Co-S, N-GQD[102]. The R_{CT} obtained from the impedance analysis for three photoelectrodes shows that cobalt in the photoelectrode structure significantly reduced the electron transfer from the electrolyte to the electrode surface and increased in current density.

Table 3-calculated charge transfer resistance by the fitting of EIS data

	C bulk ([CPE]/μF)	R_s ($\Omega\ cm^2$)	R_{ct} ($\Omega\ cm^2$)
TNR	2.11	2.38	22.4
S,N-GQD	3.96	2.78	17.1
[Co-S,N-GQD]	5.67	3.11	15.7

Scheme.2b shows the proposed mechanism for electrons and holes that photogenerated in the photoelectrochemical cell. The photons absorbed by S, N-GQD caused electrons to be excited to the compound's conduction band. With the help of the energy bandgap obtained from uv-visible analysis and the flat band energy obtained from the mott-Schottky equation, the valence band energy level of the compounds can also be obtained. A specific mechanism can be provided for how charge carriers are transported to advance the water-splitting reaction by analyzing the obtained energy levels. Since the conduction band of S, N-GQD is slightly higher than the conduction band of TiO_2 nanoarrays, the photoexcited electrons transport to the conduction band of TiO_2 and, through transfer to the substrate, transferred to the platinum electrode to conduction the proton reduction half-reaction.

On the other hand, due to the formation of the N-Co bond in the structure, the bond leads to better separation of the produced charges and faster transport to the photoelectrode surface. Due to Cobalt-pyridine compounds in the photoelectrode structure, these compounds catalyze the OER reaction. The presence of cobalt complex and pyridine ligand

dramatically improves electron transfer. On the other hand, a half-reaction of oxidation occurs when water is converted to oxygen gas and releases two electrons. It leads to an increase in the photocurrent generated in the photoelectrochemical cell.

The proposed mechanism for catalyzing the half-reaction of water oxidation was presented in the scheme.2c according to previous reports[103,104]. In the first step, the water molecule is displaced by chlorine ligands around cobalt, and an intermediate cobalt complex with five ligands is formed. Then, Co^{2+} is converted to Co^{4+} by losing two electrodes and losing two protons, and forming a double bond with oxygen by the effect of holes. The Co^{4+} formed is a perfect place for the oxidation of water. Therefore, another water molecule is absorbed by the species so that the oxidation of water occurs. After absorbing water, cobalt is converted back to Co^{2+}, releasing two electrons and two protons. In the last step, the two remaining oxygen are separated from the catalyst surface as oxygen gas. The important point in these steps is the role of the photogenerated holes to convert Co^{2+} to Co^{4+} because Co^{4+} is a strong oxidant and the main driving force of the water oxidation reaction.

Fig.12 compares the photoelectrochemical cell performance of various reports that have used TiO_2 nanostructures, GQDs or carbon dots to improve cell efficiency[105–113]. What is clear is that graphene quantum dot affects cell performance in several ways, and this combination has attracted a great deal of attention in recent years.

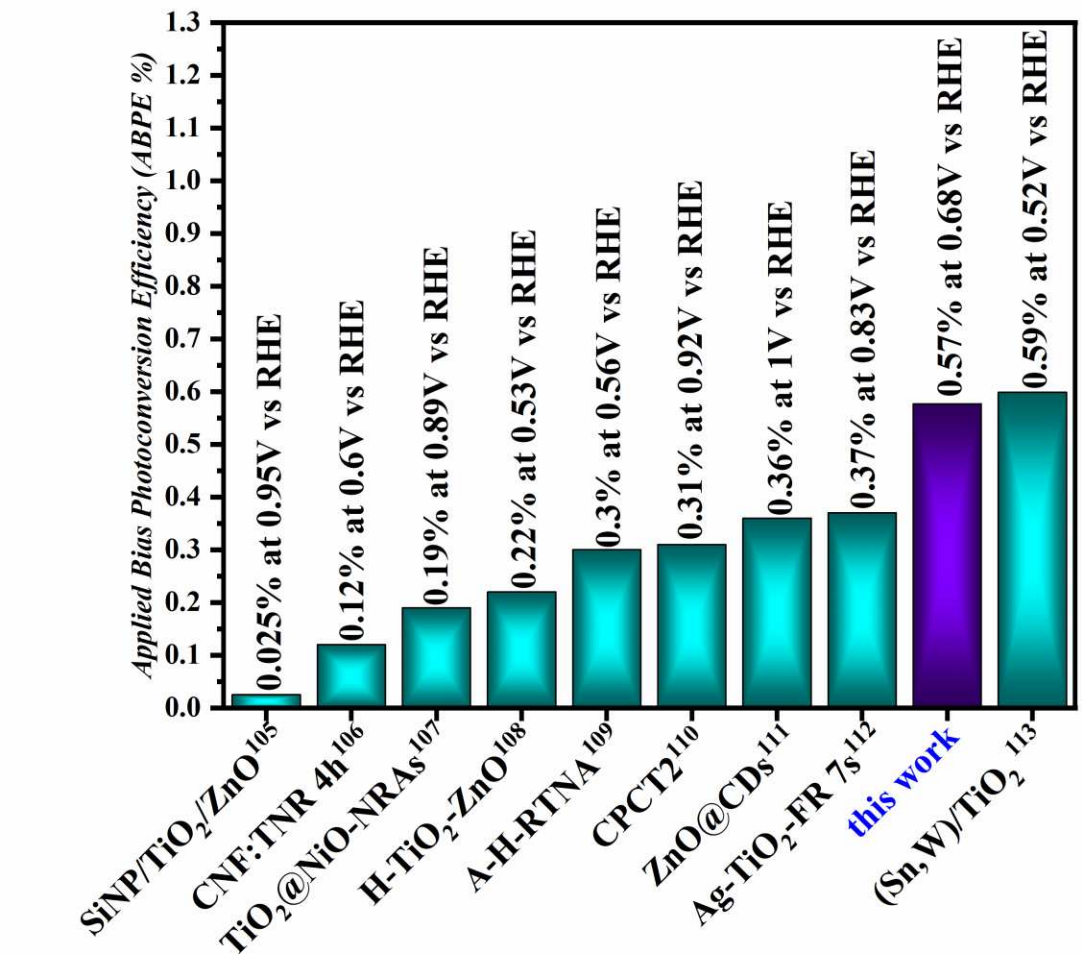

Figure 12- some recent report on TiO_2based or quantum dot-semiconductor based photoelectrode using in photoelectrochemical water splitting

4-conclusion

We proposed a new strategy in simultaneous use of the visible light absorption properties of GQD compounds and the OER reaction's catalytic properties by cobalt-pyridine complex compounds. Doping of S and N heteroatoms in GQD structure improved the optical and electronic performance. It provided the conditions for the formation of Nitrogen-Cobalt bonds within this structure. The Co-N and Co-S bands play a crucial role in enhancing the transfer characteristics and separation of charge carriers and, like Cobalt-bipyridine complexes, dramatically improves the performance of the photoelectrochemical

cell[67,114–119]. In this report, TiO_2 nanoarrays were used as semiconductors on the FTO conductive substrate. S, N-GQD was used due to the lack of absorption of visible light by TiO_2 to enhance the cell efficiency with proper absorption in the visible region. Besides, due to its high solubility in water, S, N-GQD was covalently bonded to the surface of TiO_2 nanoarrays to enhance the photoelectrode's stability. Various structural and electrochemical analyses were performed to confirm the photoelectrochemical cell's performance. The results showed the significant effect of each photoelectrode component, especially the cobalt ions structure of GQD.

Acknowledgment

The authors are grateful for the financial support of Amirkabir University of Technology (Tehran polytechnic). The calculations presented in this study were also performed using the computing facilities of the Advanced Research Computing @ Cardiff (ARCCA) division, Cardiff University, UK.

References

[1] J. Liu, W. Yang, Z. Li, F. Ren, H. Hao, Experimental investigation of thermo-physical properties of geminal dicationic ionic compounds for latent thermal energy storage, J. Mol. Liq. 307 (2020) 112994. https://doi.org/https://doi.org/10.1016/j.molliq.2020.112994.

[2] J. Tan, R. Li, S.A. Raheem, L. Pan, H. Shen, J. Liu, M. Gao, M. Yang, Facile Construction of Carbon Encapsulated of Earth-Abundant Metal Sulfides for Oxygen Electrocatalysis, ChemElectroChem. 8 (2021) 3533–3537. https://doi.org/https://doi.org/10.1002/celc.202101098.

[3] N.J. English, Electric-field-promoted photo-electrochemical production of hydrogen from water splitting, J. Mol. Liq. 342 (2021) 116949. https://doi.org/https://doi.org/10.1016/j.molliq.2021.116949.

[4] J.-X. Jian, V. Jokubavicius, M. Syväjärvi, R. Yakimova, J. Sun, Nanoporous Cubic Silicon Carbide Photoanodes for Enhanced Solar Water Splitting, ACS Nano. (2021). https://doi.org/10.1021/acsnano.1c00256.

[5] N. Sarkar, G. Sahoo, S.K. Swain, Graphene quantum dot decorated magnetic graphene oxide filled polyvinyl alcohol hybrid hydrogel for removal of dye pollutants, J. Mol. Liq. 302 (2020) 112591. https://doi.org/https://doi.org/10.1016/j.molliq.2020.112591.

[6] M. Yang, C. Wang, E. Liu, X. Hu, H. Hao, J. Fan, A novel ascorbic acid ratiometric fluorescent sensor based on ZnCdS quantum dots embedded molecularly imprinted polymer and silica-coated CdTeS quantum dots, J. Mol. Liq. 337 (2021) 116438. https://doi.org/https://doi.org/10.1016/j.molliq.2021.116438.

[7] C.-W. Tsao, M.-J. Fang, Y.-J. Hsu, Modulation of interfacial charge dynamics of semiconductor heterostructures for advanced photocatalytic applications, Coord. Chem. Rev. 438 (2021) 213876. https://doi.org/https://doi.org/10.1016/j.ccr.2021.213876.

[8] T.-H. Lai, K. Katsumata, Y.-J. Hsu, In situ charge carrier dynamics of semiconductor nanostructures for advanced photoelectrochemical and photocatalytic applications, Nanophotonics. 10 (2021) 777–795. https://doi.org/doi:10.1515/nanoph-2020-0472.

[9] Y.-H. Chiu, T.-H. Lai, M.-Y. Kuo, P.-Y. Hsieh, Y.-J. Hsu, Photoelectrochemical cells for solar hydrogen production: Challenges and opportunities, APL Mater. 7 (2019) 80901. https://doi.org/10.1063/1.5109785.

[10] P.-Y. Hsieh, J.-Y. Wu, T.-F.M. Chang, C.-Y. Chen, M. Sone, Y.-J. Hsu, Near infrared-driven photoelectrochemical water splitting: Review and future prospects, Arab. J. Chem. 13 (2020) 8372–8387. https://doi.org/https://doi.org/10.1016/j.arabjc.2020.05.025.

[11] M.-J. Fang, C.-W. Tsao, Y.-J. Hsu, Semiconductor nanoheterostructures for photoconversion applications, J. Phys. D. Appl. Phys. 53 (2020) 143001. https://doi.org/10.1088/1361-6463/ab5f25.

[12] N. Neekzad, E. Kowsari, M.D. Najafi, H. Reza Naderi, A. Chinnappan, S. Ramakrishna, V. Haddadi-Asl, Pseudocapacitive performance of surface functionalized halloysite nanotubes decorated green additive ionic liquid modified with ATP and POAP for efficient symmetric supercapacitors, J. Mol. Liq. 342 (2021) 116962. https://doi.org/https://doi.org/10.1016/j.molliq.2021.116962.

[13] Y. Li, Q. Wu, Y. Chen, R. Zhang, C. Li, K. Zhang, M. Li, Y. Lin, D. Wang, X. Zou, T. Xie, Interface engineering Z-scheme Ti-Fe2O3/In2O3 photoanode for highly efficient photoelectrochemical water splitting, Appl. Catal. B Environ. 290 (2021) 120058. https://doi.org/https://doi.org/10.1016/j.apcatb.2021.120058.

[14] X. Zhang, T. Peng, S. Song, Recent advances in dye-sensitized semiconductor

systems for photocatalytic hydrogen production, J. Mater. Chem. A. 4 (2016) 2365–2402.

[15] H. Zhou, N. Zhang, Y. Yang, J. Xue, L. Kong, Q. Zhang, R. Liu, X. Fan, C. Tao, Floating Networks of Alga-like Photoelectrodes for Highly Efficient Photoelectrochemical H2 Production, ACS Sustain. Chem. Eng. 8 (2020) 10564–10571. https://doi.org/10.1021/acssuschemeng.0c03575.

[16] S. Bibi, M. Khan, S. ur-Rehman, M. Yaseen, S. Muhammad, R. Nadeem, N. Jahan, S. Noreen, Misbah, Investigation analysis of optoelectronic and structural properties of cis- and trans-structures of azo dyes: density functional theory study, J. Phys. Org. Chem. 34 (2021) e4183. https://doi.org/https://doi.org/10.1002/poc.4183.

[17] Y.-C. Chen, K. Katsumata, Y.-H. Chiu, K. Okada, N. Matsushita, Y.-J. Hsu, ZnO–graphene composites as practical photocatalysts for gaseous acetaldehyde degradation and electrolytic water oxidation, Appl. Catal. A Gen. 490 (2015) 1–9. https://doi.org/https://doi.org/10.1016/j.apcata.2014.10.055.

[18] K.-A. Tsai, Y.-J. Hsu, Graphene quantum dots mediated charge transfer of CdSe nanocrystals for enhancing photoelectrochemical hydrogen production, Appl. Catal. B Environ. 164 (2015) 271–278. https://doi.org/https://doi.org/10.1016/j.apcatb.2014.09.034.

[19] Y.-S. Chang, M. Choi, M. Baek, P.-Y. Hsieh, K. Yong, Y.-J. Hsu, CdS/CdSe co-sensitized brookite H:TiO2 nanostructures: Charge carrier dynamics and photoelectrochemical hydrogen generation, Appl. Catal. B Environ. 225 (2018) 379–385. https://doi.org/https://doi.org/10.1016/j.apcatb.2017.11.063.

[20] Y.-H. Chiu, T.-H. Lai, C.-Y. Chen, P.-Y. Hsieh, K. Ozasa, M. Niinomi, K. Okada, T.-F.M. Chang, N. Matsushita, M. Sone, Y.-J. Hsu, Fully Depleted Ti–Nb–Ta–Zr–O Nanotubes: Interfacial Charge Dynamics and Solar Hydrogen Production, ACS Appl. Mater. Interfaces. 10 (2018) 22997–23008. https://doi.org/10.1021/acsami.8b00727.

[21] J.-M. Li, C.-W. Tsao, M.-J. Fang, C.-C. Chen, C.-W. Liu, Y.-J. Hsu, TiO2-Au-Cu2O Photocathodes: Au-Mediated Z-Scheme Charge Transfer for Efficient Solar-Driven Photoelectrochemical Reduction, ACS Appl. Nano Mater. 1 (2018) 6843–6853. https://doi.org/10.1021/acsanm.8b01678.

[22] J.-M. Li, Y.-T. Wang, Y.-J. Hsu, A more accurate, reliable method to evaluate the photoelectrochemical performance of semiconductor electrode without under/over estimation, Electrochim. Acta. 267 (2018) 141–149. https://doi.org/https://doi.org/10.1016/j.electacta.2018.02.015.

[23] P.-Y. Hsieh, Y.-H. Chiu, T.-H. Lai, M.-J. Fang, Y.-T. Wang, Y.-J. Hsu, TiO2 Nanowire-Supported Sulfide Hybrid Photocatalysts for Durable Solar Hydrogen Production, ACS Appl. Mater. Interfaces. 11 (2019) 3006–3015. https://doi.org/10.1021/acsami.8b17858.

[24] K.-A. Tsai, P.-Y. Hsieh, T.-H. Lai, C.-W. Tsao, H. Pan, Y.-G. Lin, Y.-J. Hsu, Nitrogen-Doped Graphene Quantum Dots for Remarkable Solar Hydrogen Production, ACS Appl. Energy Mater. 3 (2020) 5322–5332. https://doi.org/10.1021/acsaem.0c00335.

[25] Y.-S. Chang, P.-Y. Hsieh, T.-F. Mark Chang, C.-Y. Chen, M. Sone, Y.-J. Hsu, Incorporating graphene quantum dots to enhance the photoactivity of CdSe-sensitized TiO2 nanorods for solar hydrogen production, J. Mater. Chem. A. 8 (2020) 13971–13979. https://doi.org/10.1039/D0TA02359K.

[26] B. Bazri, Y.-C. Lin, T.-H. Lu, C.-J. Chen, E. Kowsari, S.-F. Hu, R.-S. Liu, A heteroelectrode structure for solar water splitting: integrated cobalt ditelluride across a TiO2-passivated silicon microwire array, Catal. Sci. Technol. 7 (2017) 1488–1496. https://doi.org/10.1039/C6CY02688E.

[27] S.U.M. Khan, M. Al-Shahry, W.B. Ingler, Efficient Photochemical Water Splitting by a Chemically Modified n-TiO₂, Science (80-.). 297 (2002) 2243 LP-2245. https://doi.org/10.1126/science.1075035.

[28] J. Shi, Y. Hara, C. Sun, M.A. Anderson, X. Wang, Three-Dimensional High-Density Hierarchical Nanowire Architecture for High-Performance Photoelectrochemical Electrodes, Nano Lett. 11 (2011) 3413–3419. https://doi.org/10.1021/nl201823u.

[29] W.J. Youngblood, S.-H.A. Lee, Y. Kobayashi, E.A. Hernandez-Pagan, P.G. Hoertz, T.A. Moore, A.L. Moore, D. Gust, T.E. Mallouk, Photoassisted overall water splitting in a visible light-absorbing dye-sensitized photoelectrochemical cell, J. Am. Chem. Soc. 131 (2009) 926–927.

[30] N. Seifvand, E. Kowsari, TiO2/in-situ reduced GO/functionalized with an IL-Cr complex as a ternary photocatalyst composite for efficient carbon monoxide deterioration from air, Appl. Catal. B Environ. 206 (2017) 184–193.

[31] E. Kowsari, M.R. Chirani, High efficiency dye-sensitized solar cells with tetra alkyl ammonium cation-based ionic liquid functionalized graphene oxide as a novel additive in nanocomposite electrolyte, Carbon N. Y. 118 (2017) 384–392. https://doi.org/https://doi.org/10.1016/j.carbon.2017.03.074.

[32] S.T.R. Naqvi, T. Rasheed, S. Majeed, Z. Rani, R. Nawaz, M.N. Ashiq, Development of nitrogen doped carbon dots modified CuCo alloy nanoparticles for

potential electrocatalytic water splitting, J. Mol. Liq. 309 (2020) 113111. https://doi.org/https://doi.org/10.1016/j.molliq.2020.113111.

[33] R. Reichert, Z. Jusys, R.J. Behm, Au/TiO2 photo (electro) catalysis: the role of the Au cocatalyst in photoelectrochemical water splitting and photocatalytic H2 evolution, J. Phys. Chem. C. 119 (2015) 24750–24759.

[34] T. Zhou, J. Wang, S. Chen, J. Bai, J. Li, Y. Zhang, L. Li, L. Xia, M. Rahim, Q. Xu, B. Zhou, Bird-nest structured ZnO/TiO2 as a direct Z-scheme photoanode with enhanced light harvesting and carriers kinetics for highly efficient and stable photoelectrochemical water splitting, Appl. Catal. B Environ. 267 (2020) 118599. https://doi.org/https://doi.org/10.1016/j.apcatb.2020.118599.

[35] M. Altomare, K. Lee, M.S. Killian, E. Selli, P. Schmuki, Ta-doped TiO2 nanotubes for enhanced solar-light photoelectrochemical water splitting, Chem. Eur. J. 19 (2013) 5841–5844.

[36] A.A. Ashtiani, E. Kowsari, V. Haddadi-Asl, M. Yousefi, H.R. Naderi, A. Chinnappan, S. Ramakrishna, Pseudocapacitive efficiency of covalently Cr-complex with L-histidine-methyl ester as a ligand graphene oxide blended with conducting polymer (POAP) as electrode material in supercapacitor, J. Mol. Liq. 315 (2020) 113697. https://doi.org/https://doi.org/10.1016/j.molliq.2020.113697.

[37] X. Feng, K. Shankar, O.K. Varghese, M. Paulose, T.J. Latempa, C.A. Grimes, Vertically Aligned Single Crystal TiO2 Nanowire Arrays Grown Directly on Transparent Conducting Oxide Coated Glass: Synthesis Details and Applications, Nano Lett. 8 (2008) 3781–3786. https://doi.org/10.1021/nl802096a.

[38] J.W. Yoon, D.H. Kim, J.-H. Kim, H.W. Jang, J.-H. Lee, NH2-MIL-125(Ti)/TiO2 nanorod heterojunction photoanodes for efficient photoelectrochemical water splitting, Appl. Catal. B Environ. 244 (2019) 511–518. https://doi.org/https://doi.org/10.1016/j.apcatb.2018.11.057.

[39] B. Liu, E.S. Aydil, Growth of Oriented Single-Crystalline Rutile TiO2 Nanorods on Transparent Conducting Substrates for Dye-Sensitized Solar Cells, J. Am. Chem. Soc. 131 (2009) 3985–3990. https://doi.org/10.1021/ja8078972.

[40] J. Park, P.R. Deshmukh, Y. Sohn, W.G. Shin, ZnO-TiO2 core-shell nanowires decorated with Au nanoparticles for plasmon-enhanced photoelectrochemical water splitting, J. Alloys Compd. 787 (2019) 1310–1319. https://doi.org/https://doi.org/10.1016/j.jallcom.2019.02.061.

[41] J.R. Swierk, N.S. McCool, C.T. Nemes, T.E. Mallouk, C.A. Schmuttenmaer, Ultrafast Electron Injection Dynamics of Photoanodes for Water-Splitting Dye-Sensitized Photoelectrochemical Cells, J. Phys. Chem. C. 120 (2016) 5940–5948.

https://doi.org/10.1021/acs.jpcc.6b00749.

[42] S. Alhammadi, B.G. Mun, S. Gedi, V.R. Minnam Reddy, A.M. Rabie, M.S. Sayed, J.-J. Shim, H. Park, W.K. Kim, Effect of silver doping on the properties and photocatalytic performance of In2S3 nanoparticles, J. Mol. Liq. 344 (2021) 117649. https://doi.org/https://doi.org/10.1016/j.molliq.2021.117649.

[43] M. Dutta, S. Sarkar, T. Ghosh, D. Basak, ZnO/Graphene Quantum Dot Solid-State Solar Cell, J. Phys. Chem. C. 116 (2012) 20127–20131. https://doi.org/10.1021/jp302992k.

[44] M. Yang, Y. Yan, E. Liu, X. Hu, H. Hao, J. Fan, Polyethyleneimine-functionalized carbon dots as a fluorescent probe for doxorubicin hydrochloride by an inner filter effect, Opt. Mater. (Amst). 112 (2021) 110743. https://doi.org/https://doi.org/10.1016/j.optmat.2020.110743.

[45] D. Bharatiya, B. Parhi, S.K. Swain, Preparation, characterization and dielectric properties of GO based ZnO embedded mixed metal oxides ternary nanostructured composites, J. Alloys Compd. 869 (2021) 159274. https://doi.org/https://doi.org/10.1016/j.jallcom.2021.159274.

[46] Y. Duan, X. Zhao, M. Sun, H. Hao, Research Advances in the Synthesis, Application, Assembly, and Calculation of Janus Materials, Ind. Eng. Chem. Res. 60 (2021) 1071–1095. https://doi.org/10.1021/acs.iecr.0c04304.

[47] I. Son, S.-R. Son, J. An, J.-W. Choi, S. Kim, W.Y. Lee, J.H. Lee, Photoluminescent surface-functionalized graphene quantum dots for spontaneous interfacial homeotropic orientation of liquid crystals, J. Mol. Liq. 332 (2021) 115901. https://doi.org/https://doi.org/10.1016/j.molliq.2021.115901.

[48] H. Teymourinia, M. Salavati-Niasari, O. Amiri, M. Farangi, Facile synthesis of graphene quantum dots from corn powder and their application as down conversion effect in quantum dot-dye-sensitized solar cell, J. Mol. Liq. 251 (2018) 267–272. https://doi.org/https://doi.org/10.1016/j.molliq.2017.12.059.

[49] W. Lv, T. Shen, F. Ding, S. Mao, Z. Ma, J. Xie, M. Gao, A novel NH2-rich polymer/graphene oxide/organo-vermiculite adsorbent for the efficient removal of azo dyes, J. Mol. Liq. 341 (2021) 117308. https://doi.org/https://doi.org/10.1016/j.molliq.2021.117308.

[50] M. Mohamadi, E. Kowsari, V. Haddadi-Asl, M. Yousefzadeh, Fabrication, characterization and electromagnetic wave absorption properties of covalently modified reduced graphene oxide based on dinuclear cobalt complex, Compos. Part B Eng. 162 (2019) 569–579. https://doi.org/https://doi.org/10.1016/j.compositesb.2019.01.032.

[51] N. Sarkar, G. Sahoo, S.K. Swain, Reduced graphene oxide decorated superporous polyacrylamide based interpenetrating network hydrogel as dye adsorbent, Mater. Chem. Phys. 250 (2020) 123022. https://doi.org/https://doi.org/10.1016/j.matchemphys.2020.123022.

[52] S. Abdpour, E. Kowsari, B. Bazri, M.R.A. Moghaddam, S.S. Tafreshi, N.H. de Leeuw, I. Simon, L. Schmolke, D. Dietrich, S. Ramakrishna, C. Janiak, Amino-functionalized MIL-101(Cr) photodegradation enhancement by sulfur-enriched copper sulfide nanoparticles: An experimental and DFT study, J. Mol. Liq. 319 (2020) 114341. https://doi.org/https://doi.org/10.1016/j.molliq.2020.114341.

[53] S. Mao, M. Gao, Functional organoclays for removal of heavy metal ions from water: A review, J. Mol. Liq. 334 (2021) 116143. https://doi.org/https://doi.org/10.1016/j.molliq.2021.116143.

[54] Y. Xiang, M. Gao, T. Shen, G. Cao, B. Zhao, S. Guo, Comparative study of three novel organo-clays modified with imidazolium-based gemini surfactant on adsorption for bromophenol blue, J. Mol. Liq. 286 (2019) 110928. https://doi.org/https://doi.org/10.1016/j.molliq.2019.110928.

[55] S. Perveen, R. Nadeem, M. Iqbal, S. Bibi, R. Gill, R. Saeed, S. Noreen, K. Akhtar, T. Mehmood Ansari, N. Alfryyan, Graphene oxide and Fe3O4 composite synthesis, characterization and adsorption efficiency evaluation for $NO3^{-}$ and $PO43^{-}$ ions in aqueous medium, J. Mol. Liq. 339 (2021) 116746. https://doi.org/https://doi.org/10.1016/j.molliq.2021.116746.

[56] S. Noreen, M. Tahira, M. Ghamkhar, I. Hafiz, H.N. Bhatti, R. Nadeem, M.A. Murtaza, M. Yaseen, A.A. Sheikh, Z. Naseem, F. Younas, Treatment of textile wastewater containing acid dye using novel polymeric graphene oxide nanocomposites (GO/PAN,GO/PPy, GO/PSty), J. Mater. Res. Technol. 14 (2021) 25–35. https://doi.org/https://doi.org/10.1016/j.jmrt.2021.06.007.

[57] L. Li, H. Wu, J. Chen, L. Xu, G. Sheng, P. Fang, K. Du, C. Shen, X. Guo, Anchoring nanoscale iron sulfide onto graphene oxide for the highly efficient immobilization of uranium (VI) from aqueous solutions, J. Mol. Liq. 332 (2021) 115910. https://doi.org/https://doi.org/10.1016/j.molliq.2021.115910.

[58] J. Chen, H. Wu, L. Xu, M. Li, K. Du, G. Sheng, New insights into colloidal GO, Cr(VI) and Fe(II) interaction by a combined batch, spectroscopic and DFT calculation investigation, J. Mol. Liq. 337 (2021) 116365. https://doi.org/https://doi.org/10.1016/j.molliq.2021.116365.

[59] T.-F. Yeh, C.-Y. Teng, S.-J. Chen, H. Teng, Nitrogen-Doped Graphene Oxide Quantum Dots as Photocatalysts for Overall Water-Splitting under Visible Light

Illumination, Adv. Mater. 26 (2014) 3297–3303. https://doi.org/https://doi.org/10.1002/adma.201305299.

[60] W.D. Chemelewski, H.-C. Lee, J.-F. Lin, A.J. Bard, C.B. Mullins, Amorphous FeOOH Oxygen Evolution Reaction Catalyst for Photoelectrochemical Water Splitting, J. Am. Chem. Soc. 136 (2014) 2843–2850. https://doi.org/10.1021/ja411835a.

[61] X. Liang, S. Yang, J. Yang, W. Sun, X. Li, B. Ma, J. Huang, J. Zhang, L. Duan, Y. Ding, Covalent immobilization of molecular complexes on metal-organic frameworks towards robust and highly efficient heterogeneous water oxidation catalysts, Appl. Catal. B Environ. 291 (2021) 120070. https://doi.org/https://doi.org/10.1016/j.apcatb.2021.120070.

[62] H. Wu, J. Chen, L. Xu, X. Guo, P. Fang, K. Du, C. Shen, G. Sheng, Decorating nanoscale FeS onto metal-organic framework for the decontamination performance and mechanism of Cr(VI) and Se(IV), Colloids Surfaces A Physicochem. Eng. Asp. 625 (2021) 126887. https://doi.org/https://doi.org/10.1016/j.colsurfa.2021.126887.

[63] C. Bathula, A. Talha Aqueel Ahmed, A. Kadam, S. Sekar, J.-H. Hwang, S.-H. Lee, H.-S. Kim, Multi-functional Co3O4 embedded carbon nanotube architecture for oxygen evolution reaction and benzoin oxidation, J. Mol. Liq. 343 (2021) 117616. https://doi.org/https://doi.org/10.1016/j.molliq.2021.117616.

[64] C.-F. Leung, S.-M. Ng, C.-C. Ko, W.-L. Man, J. Wu, L. Chen, T.-C. Lau, A cobalt (II) quaterpyridine complex as a visible light-driven catalyst for both water oxidation and reduction, Energy Environ. Sci. 5 (2012) 7903–7907.

[65] D. Hong, J. Jung, J. Park, Y. Yamada, T. Suenobu, Y.-M. Lee, W. Nam, S. Fukuzumi, Water-soluble mononuclear cobalt complexes with organic ligands acting as precatalysts for efficient photocatalytic water oxidation, Energy Environ. Sci. 5 (2012) 7606–7616. https://doi.org/10.1039/C2EE21185H.

[66] L. Duan, Y. Xu, P. Zhang, M. Wang, L. Sun, Visible Light-Driven Water Oxidation by a Molecular Ruthenium Catalyst in Homogeneous System, Inorg. Chem. 49 (2010) 209–215. https://doi.org/10.1021/ic9017486.

[67] X. Zhou, T. Zhang, C.W. Abney, Z. Li, W. Lin, Graphene-Immobilized Monomeric Bipyridine-Mx+ (Mx+ = Fe3+, Co2+, Ni2+, or Cu2+) Complexes for Electrocatalytic Water Oxidation, ACS Appl. Mater. Interfaces. 6 (2014) 18475–18479. https://doi.org/10.1021/am506435u.

[68] X. Hu, X.-J. Zheng, Y. Li, D.-K. Ma, Bipyridine-Co2+ molecular catalyst modified WO3 nanoplate arrays photoanode with enhanced photoelectrochemical activity,

Mater. Lett. 220 (2018) 36–39.

[69] D. Bharatiya, S. Patra, B. Parhi, S.K. Swain, A materials science approach towards bioinspired polymeric nanocomposites: a comprehensive review, Int. J. Polym. Mater. Polym. Biomater. (2021) 1–16. https://doi.org/10.1080/00914037.2021.1990057.

[70] M. Wang, Y.-S. Chang, C.-W. Tsao, M.-J. Fang, Y.-J. Hsu, K.-L. Choy, Enhanced photoelectrochemical hydrogen generation in neutral electrolyte using non-vacuum processed CIGS photocathodes with an earth-abundant cobalt sulfide catalyst, Chem. Commun. 55 (2019) 2465–2468. https://doi.org/10.1039/C8CC09426H.

[71] D. Qu, M. Zheng, P. Du, Y. Zhou, L. Zhang, D. Li, H. Tan, Z. Zhao, Z. Xie, Z. Sun, Highly luminescent S, N co-doped graphene quantum dots with broad visible absorption bands for visible light photocatalysts, Nanoscale. 5 (2013) 12272–12277.

[72] W. Kohn, L.J. Sham, Self-Consistent Equations Including Exchange and Correlation Effects, Phys. Rev. 140 (1965) A1133–A1138. https://doi.org/10.1103/PhysRev.140.A1133.

[73] P. Hohenberg, W. Kohn, Inhomogeneous Electron Gas, Phys. Rev. 136 (1964) B864–B871. https://doi.org/10.1103/PhysRev.136.B864.

[74] G. Kresse, J. Furthmüller, Efficiency of ab-initio total energy calculations for metals and semiconductors using a plane-wave basis set, Comput. Mater. Sci. 6 (1996) 15–50. https://doi.org/https://doi.org/10.1016/0927-0256(96)00008-0.

[75] G. Kresse, J. Furthmüller, Efficient iterative schemes for ab initio total-energy calculations using a plane-wave basis set, Phys. Rev. B. 54 (1996) 11169–11186. https://doi.org/10.1103/PhysRevB.54.11169.

[76] J.P. Perdew, K. Burke, M. Ernzerhof, Generalized Gradient Approximation Made Simple, Phys. Rev. Lett. 77 (1996) 3865–3868. https://doi.org/10.1103/PhysRevLett.77.3865.

[77] J. Paier, R. Hirschl, M. Marsman, G. Kresse, The Perdew–Burke–Ernzerhof exchange-correlation functional applied to the G2-1 test set using a plane-wave basis set, J. Chem. Phys. 122 (2005) 234102. https://doi.org/10.1063/1.1926272.

[78] P.E. Blöchl, Projector augmented-wave method, Phys. Rev. B. 50 (1994) 17953–17979. https://doi.org/10.1103/PhysRevB.50.17953.

[79] A.I. Liechtenstein, V.I. Anisimov, J. Zaanen, Density-functional theory and strong interactions: Orbital ordering in Mott-Hubbard insulators, Phys. Rev. B. 52 (1995)

R5467–R5470. https://doi.org/10.1103/PhysRevB.52.R5467.

[80] A. V Krukau, O.A. Vydrov, A.F. Izmaylov, G.E. Scuseria, Influence of the exchange screening parameter on the performance of screened hybrid functionals, J. Chem. Phys. 125 (2006) 224106. https://doi.org/10.1063/1.2404663.

[81] Q. Huang, G. Zhou, L. Fang, L. Hu, Z.-S. Wang, TiO2 nanorod arrays grown from a mixed acid medium for efficient dye-sensitized solar cells, Energy Environ. Sci. 4 (2011) 2145–2151. https://doi.org/10.1039/C1EE01166A.

[82] T. Rahimi-Aghdam, Z. Shariatinia, M. Hakkarainen, V. Haddadi-Asl, Nitrogen and phosphorous doped graphene quantum dots: Excellent flame retardants and smoke suppressants for polyacrylonitrile nanocomposites, J. Hazard. Mater. 381 (2020) 121013. https://doi.org/https://doi.org/10.1016/j.jhazmat.2019.121013.

[83] S. Gu, C.-T. Hsieh, Y.-Y. Tsai, Y. Ashraf Gandomi, S. Yeom, K.D. Kihm, C.-C. Fu, R.-S. Juang, Sulfur and Nitrogen Co-Doped Graphene Quantum Dots as a Fluorescent Quenching Probe for Highly Sensitive Detection toward Mercury Ions, ACS Appl. Nano Mater. 2 (2019) 790–798. https://doi.org/10.1021/acsanm.8b02010.

[84] D. Huang, J. Lu, S. Li, Y. Luo, C. Zhao, B. Hu, M. Wang, Y. Shen, Fabrication of Cobalt Porphyrin. Electrochemically Reduced Graphene Oxide Hybrid Films for Electrocatalytic Hydrogen Evolution in Aqueous Solution, Langmuir. 30 (2014) 6990–6998. https://doi.org/10.1021/la501052m.

[85] J. Hu, D. Chen, N. Li, Q. Xu, H. Li, J. He, J. Lu, Fabrication of graphitic-C3N4 quantum dots/graphene-InVO4 aerogel hybrids with enhanced photocatalytic NO removal under visible-light irradiation, Appl. Catal. B Environ. 236 (2018) 45–52. https://doi.org/https://doi.org/10.1016/j.apcatb.2018.04.080.

[86] W. Deng, H. Jiang, C. Chen, L. Yang, Y. Zhang, S. Peng, S. Wang, Y. Tan, M. Ma, Q. Xie, Co-, N-, and S-Tridoped Carbon Derived from Nitrogen- and Sulfur-Enriched Polymer and Cobalt Salt for Hydrogen Evolution Reaction, ACS Appl. Mater. Interfaces. 8 (2016) 13341–13347. https://doi.org/10.1021/acsami.5b12666.

[87] L. Wang, W. Zhang, X. Zheng, Y. Chen, W. Wu, J. Qiu, X. Zhao, X. Zhao, Y. Dai, J. Zeng, Incorporating nitrogen atoms into cobalt nanosheets as a strategy to boost catalytic activity toward CO2 hydrogenation, Nat. Energy. 2 (2017) 869–876. https://doi.org/10.1038/s41560-017-0015-x.

[88] P. Yang, R. Wang, H. Tao, Y. Zhang, M.-M. Titirici, X. Wang, Cobalt Nitride Anchored on Nitrogen-Rich Carbons for Efficient Carbon Dioxide Reduction with Visible Light, Appl. Catal. B Environ. 280 (2021) 119454. https://doi.org/https://doi.org/10.1016/j.apcatb.2020.119454.

[89] R. V Khose, P. Bangde, M.P. Bondarde, P.S. Dhumal, M.A. Bhakare, G. Chakraborty, A.K. Ray, P. Dandekar, S. Some, Waste derived approach towards wealthy fluorescent N-doped graphene quantum dots for cell imaging and H2O2 sensing applications, Spectrochim. Acta Part A Mol. Biomol. Spectrosc. 266 (2022) 120453. https://doi.org/https://doi.org/10.1016/j.saa.2021.120453.

[90] A. Singh, S. Kumar, A.K. Ojha, Charcoal derived graphene quantum dots for flexible supercapacitor oriented applications, New J. Chem. 44 (2020) 11085–11091. https://doi.org/10.1039/D0NJ00899K.

[91] R. V Khose, G. Chakraborty, M.P. Bondarde, P.H. Wadekar, A.K. Ray, S. Some, Red-fluorescent graphene quantum dots from guava leaf as a turn-off probe for sensing aqueous Hg(ii), New J. Chem. 45 (2021) 4617–4625. https://doi.org/10.1039/D0NJ06259F.

[92] P. Luo, X. Guan, Y. Yu, X. Li, F. Yan, Hydrothermal Synthesis of Graphene Quantum Dots Supported on Three-Dimensional Graphene for Supercapacitors, Nanomater. . 9 (2019). https://doi.org/10.3390/nano9020201.

[93] W.-K. Jo, S. Moru, S. Tonda, Cobalt-Coordinated Sulfur-Doped Graphitic Carbon Nitride on Reduced Graphene Oxide: An Efficient Metal–(N,S)–C-Class Bifunctional Electrocatalyst for Overall Water Splitting in Alkaline Media, ACS Sustain. Chem. Eng. 7 (2019) 15373–15384. https://doi.org/10.1021/acssuschemeng.9b02705.

[94] C. Hu, J. Liu, J. Wang, W. She, J. Xiao, J. Xi, Z. Bai, S. Wang, Coordination-Assisted Polymerization of Mesoporous Cobalt Sulfide/Heteroatom (N,S)-Doped Double-Layered Carbon Tubes as an Efficient Bifunctional Oxygen Electrocatalyst, ACS Appl. Mater. Interfaces. 10 (2018) 33124–33134. https://doi.org/10.1021/acsami.8b07343.

[95] P. Chen, K. Li, Y. Yu, W. Zhang, Applied Surface Science Cobalt-doped graphitic carbon nitride photocatalysts with high activity for hydrogen evolution, Appl. Surf. Sci. 392 (2017) 608–615. https://doi.org/10.1016/j.apsusc.2016.09.086.

[96] B. Bazri, E. Kowsari, N. Seifvand, N. Naseri, RGO-α-Fe2O3/β-FeOOH ternary heterostructure with urchin-like morphology for efficient oxygen evolution reaction, J. Electroanal. Chem. 843 (2019) 1–11. https://doi.org/https://doi.org/10.1016/j.jelechem.2019.04.069.

[97] S. Wang, X. Bao, B. Gao, M. Li, A novel sulfur quantum dot for the detection of cobalt ions and norfloxacin as a fluorescent “switch,” Dalt. Trans. 48 (2019) 8288–8296. https://doi.org/10.1039/C9DT01186B.

[98] G. Rajender, P.K. Giri, Formation mechanism of graphene quantum dots and their

edge state conversion probed by photoluminescence and Raman spectroscopy, J. Mater. Chem. C. 4 (2016) 10852–10865. https://doi.org/10.1039/C6TC03469A.

[99] A. Lerf, H. He, M. Forster, J. Klinowski, Structure of Graphite Oxide Revisited, J. Phys. Chem. B. 102 (1998) 4477–4482. https://doi.org/10.1021/jp9731821.

[100] D. Cahen, G. Hodes, M. Grätzel, J.F. Guillemoles, I. Riess, Nature of Photovoltaic Action in Dye-Sensitized Solar Cells, J. Phys. Chem. B. 104 (2000) 2053–2059. https://doi.org/10.1021/jp993187t.

[101] V. Sharma, P.K. Jha, Enhancement in power conversion efficiency of edge-functionalized graphene quantum dot through adatoms for solar cell applications, Sol. Energy Mater. Sol. Cells. 200 (2019) 109908. https://doi.org/https://doi.org/10.1016/j.solmat.2019.04.030.

[102] Y.-H. Chiu, K.-D. Chang, Y.-J. Hsu, Plasmon-mediated charge dynamics and photoactivity enhancement for Au-decorated ZnO nanocrystals, J. Mater. Chem. A. 6 (2018) 4286–4296. https://doi.org/10.1039/C7TA08543E.

[103] D.J. Wasylenko, C. Ganesamoorthy, J. Borau-Garcia, C.P. Berlinguette, Electrochemical evidence for catalyticwater oxidation mediated by a high-valent cobalt complex, Chem. Commun. 47 (2011) 4249–4251. https://doi.org/10.1039/C0CC05522K.

[104] Z.-Q. Wang, L.-Z. Tang, Y.-X. Zhang, S.-Z. Zhan, J.-S. Ye, Electrochemical-driven water splitting catalyzed by a water-soluble cobalt(II) complex supported by N,N′-bis(2′-pyridinecarboxamide)-1,2-benzene with high turnover frequency, J. Power Sources. 287 (2015) 50–57. https://doi.org/https://doi.org/10.1016/j.jpowsour.2015.04.031.

[105] M. Pavlenko, K. Siuzdak, E. Coy, K. Załęski, M. Jancelewicz, I. Iatsunskyi, Enhanced solar-driven water splitting of 1D core-shell Si/TiO2/ZnO nanopillars, Int. J. Hydrogen Energy. 45 (2020) 26426–26433. https://doi.org/https://doi.org/10.1016/j.ijhydene.2019.11.231.

[106] P. Kumar, U.K. Thakur, K. Alam, P. Kar, R. Kisslinger, S. Zeng, S. Patel, K. Shankar, Arrays of TiO2 nanorods embedded with fluorine doped carbon nitride quantum dots (CNFQDs) for visible light driven water splitting, Carbon N. Y. 137 (2018) 174–187. https://doi.org/https://doi.org/10.1016/j.carbon.2018.05.019.

[107] N. Zheng, X. He, W. Guo, Z. Hu, Enhancement of mass transfer efficiency and photoelectrochemical activity for TiO2 nanorod arrays by decorating Ni3+-states functional NiO water oxidation cocatalyst, Chinese Chem. Lett. 32 (2021) 1993–1997. https://doi.org/https://doi.org/10.1016/j.cclet.2020.10.039.

[108] C.-C. Wang, C.-Y. Chou, S.-R. Yi, H.-D. Chen, Deposition of heterojunction of ZnO on hydrogenated TiO2 nanotube arrays by atomic layer deposition for enhanced photoelectrochemical water splitting, Int. J. Hydrogen Energy. 44 (2019) 28685–28697. https://doi.org/https://doi.org/10.1016/j.ijhydene.2019.09.133.

[109] J. Hu, S. Zhang, Y. Cao, H. Wang, H. Yu, F. Peng, Novel Highly Active Anatase/Rutile TiO2 Photocatalyst with Hydrogenated Heterophase Interface Structures for Photoelectrochemical Water Splitting into Hydrogen, ACS Sustain. Chem. Eng. 6 (2018) 10823–10832. https://doi.org/10.1021/acssuschemeng.8b02130.

[110] Z. Yu, Y. Li, J. Qu, R. Zheng, J.M. Cairney, J. Zhang, M. Zhu, A. Khan, W. Li, Enhanced photoelectrochemical water-splitting performance with a hierarchical heterostructure: Co3O4 nanodots anchored TiO2@P-C3N4 core-shell nanorod arrays, Chem. Eng. J. 404 (2021) 126458. https://doi.org/https://doi.org/10.1016/j.cej.2020.126458.

[111] X. Xu, Z. Bao, W. Tang, H. Wu, J. Pan, J. Hu, H. Zeng, Surface states engineering carbon dots as multi-band light active sensitizers for ZnO nanowire array photoanode to boost solar water splitting, Carbon N. Y. 121 (2017) 201–208. https://doi.org/https://doi.org/10.1016/j.carbon.2017.05.095.

[112] B. Chen, X. Chen, R. Li, W. Fan, F. Wang, B. Mao, W. Shi, Flame Reduced TiO2 Nanorod Arrays with Ag Nanoparticle Decoration for Efficient Solar Water Splitting, Ind. Eng. Chem. Res. 58 (2019) 4818–4827. https://doi.org/10.1021/acs.iecr.8b06171.

[113] B. Chen, B. Ge, S. Fu, Q. Li, X. Chen, L. Li, J. Wang, Z. Yang, J. Ding, W. Fan, B. Mao, W. Shi, Ex-situ flame co-doping of tin and tungsten ions in TiO2 nanorod arrays for synergistic promotion of solar water splitting, Chem. Eng. Sci. 226 (2020) 115843. https://doi.org/https://doi.org/10.1016/j.ces.2020.115843.

[114] Y. Sasaki, H. Kato, A. Kudo, [Co(bpy)3]3+/2+ and [Co(phen)3]3+/2+ Electron Mediators for Overall Water Splitting under Sunlight Irradiation Using Z-Scheme Photocatalyst System, J. Am. Chem. Soc. 135 (2013) 5441–5449. https://doi.org/10.1021/ja400238r.

[115] C. Prasad, H. Tang, Q.Q. Liu, S. Zulfiqar, S. Shah, I. Bahadur, An overview of semiconductors/layered double hydroxides composites: Properties, synthesis, photocatalytic and photoelectrochemical applications, J. Mol. Liq. 289 (2019) 111114. https://doi.org/https://doi.org/10.1016/j.molliq.2019.111114.

[116] M.R. Chirani, E. Kowsari, H. SalarAmoli, M. Yousefzadeh, A. Chinnappan, S. Ramakrishna, Covalently functionalized graphene oxide with cobalt–nitrogen-

enriched complex containing iodide ligand as charge carrier nanofiller for eco-friendly high performance ionic liquid-based dye-sensitized solar cell, J. Mol. Liq. 325 (2021) 115198. https://doi.org/https://doi.org/10.1016/j.molliq.2020.115198.

[117] F. Boorboor Ajdari, M. Dashti Najafi, M. Izadpanah Ostad, H. reza Naderi, M. Niknam Shahrak, E. Kowsari, S. Ramakrishna, A symmetric ZnO-ZIF8//Mo-ZIF8 supercapacitor and comparing with electrochemical of Pt, Au, and Cu decorated ZIF-8 electrodes, J. Mol. Liq. 333 (2021) 116007. https://doi.org/https://doi.org/10.1016/j.molliq.2021.116007.

[118] R. Mangiri, D.A. Reddy, K. Subramanyam, K.S. Kumar, A. Sudharani, B. Poornaprakash, R.P. Vijayalakshmi, Decorating MoS2 and CoSe2 nanostructures on 1D-CdS nanorods for boosting photocatalytic hydrogen evolution rate, J. Mol. Liq. 289 (2019) 111164. https://doi.org/https://doi.org/10.1016/j.molliq.2019.111164.

[119] M. Yang, C. Wang, Y. Yan, E. Liu, X. Hu, H. Hao, J. Fan, Visual detection of folic acid based on silica coated CdTeS quantum dots in serum samples, Mater. Res. Bull. 144 (2021) 111509. https://doi.org/https://doi.org/10.1016/j.materresbull.2021.111509.